CHAPTER 5

Chapter-5

Petrography & Geochemistry

Petrographic and geochemical studies help in unravelling the textural relationship, protolith history, and probable tectonic setting of a rock suite. Selected samples from both the basement granitoid and Srisailam Formation have been subjected to rigorous petrographic and geochemical studies to understand the evolutionary history of the rock sequence in the Chitrial area. For petrographic studies, 50 slides from basement granitoids and 10 slides from Srisailam sediments have been studied. For geochemical work, major element geochemistry was carried out from 28 samples of basement granitoids and 8 samples of Srisailam sandstone using X-ray fluorescence techniques. Trace element and rare Earth element (REE) geochemistry was carried out from 7 basement granitoid samples and 5 Srisailam sandstone samples by Laser Ablation- Inductively Coupled Plasma Mass Spectrometer (LA-ICP-MS). Locations of the samples (both from basement and cover sediments) which have been chosen for geochemical analysis are shown in Figure 5.1.

5.1 Analytical method

To understand the mineralogical evolution of the Chitrial outlier, petrographic study of the basement and cover rocks were carried out (Table 5.1). For petrographic study, both polarized light microscopy and scanning electron microscopy were used.

Primarily, for optical microscopy, a Nikon Eclipse LV100 research model polarizing microscope fitted with digital camera was used and images were processed with Nikon NIS-Elements image processing software. For detailed and advanced microscopic study, scanning electron microscopy was carried out. For that, a TESCAN Vega LSU scanning electron microscope fitted with Oxford Instruments X-act EDS facility was used at the Presidency University. Back Scatter Electron (BSE) imaging was done for all critical microdomains to understand the fine textural details involving grain boundary relationship, grain morphology and development of ore minerals in micro/nanometre scale, whereas the semi-quantitative analysis of different minerals phases were acquired using INCA software calibrated with the EDS attachment. The instrument was operated with 20 KV acceleration voltage.

Selected samples were analysed for major and trace elements using both XRF and ICP-MS method. Whole-rock geochemical analyses for major and trace elements of selected samples were carried out by X-ray fluorescence techniques using a Rigaku ZXS system at Hiroshima University, Japan. For whole rock chemical analysis, representative samples were cleaned with deionized water and

crushed using Jaw Crusher to smaller chip size. Subsequently, these samples were fused into glass discs using an oven-dried alkali flux, Johnson Matthery Spectroflux 100B [a mixture of lithium tetraborate ($Li_2B_4O_7$) and lithium metaborate ($LiBO_2$) with a mixing ratio of 2:8] and lithium nitrate ($LiNO_3$) as oxidising agent. The discs were prepared from 2.0 gm of rock powder, 4.0 gm of flux and 0.60 gm of $LiNO_3$ as an oxidizer and ~100 μL of 5% LiI solution added to prevent adhesion to the Pt crucible. X-rays generated by a 3kW Rh-W dual anode tube were radiated on fused bead samples. LOI are calculated after baking the powdered sample successively at 120°C for 24 hours and 900°C for 6 hours. The analytical precision (1σ) of major elements measured in XRF ranges between 0.001 and 0.14 wt%, while that for minor elements ranges between 0.68 to 2.39 ppm (Kanazawa et al., 2001). A second batch of samples was analyzed using the Panalytical Axios^{mAX} XRF system at Presidency University.

REE analysis for the selected samples was done in two sessions. The first session of analysis was done with Laser Ablation- Inductively Coupled Plasma Mass Spectrometer (LA-ICPMS) at Hiroshima University, Japan using 213 nm Nd-YAG Laser (New Wave ResearchUP-213) coupled with Agilent 7500 ICP-MS. Analyses were carried out on glass of the same powdered samples for trace elements and rare-Earth element concentrations. NIST610 glass using same ratio of sample and flux was also measured as standard sample before and after each unknown analysis. Blank glass was also measured for REE-content (though very low) correction. The details of the analytical protocols are same as in Saha *et al*. (2016). The error limits for REE range between 2 and 5%. The second session of

analysis was carried out from the Bureau Veritas (ACME lab), Canada. For trace elements and REE, a PerkinElmer ELAN 9000 ICP-MS. Samples were digested using lithium tetraborate fusion. Prepared sample is mixed with $LiBO_2/Li_2B_4O_7$ flux. Crucibles are fused in a furnace. The cooled bead is dissolved in ACS grade nitric acid and analyzed by ICP-MS. Loss on ignition (LOI) was determined by igniting a sample split then measuring the weight loss. Total Carbon and Sulphur may be included and is determined by the Leco method (TC003).

5.2 Geochemistry and petrogenesis of the granitoids

Granite is the major component of basement rocks within which massive grey granite, massive pink granite, granite gneiss, and porphyritic granite are common. An older greenstone belt known as Peddavura schist belt occurs as enclave within granite. This schist belt is considered to be equivalent of Late Archean Greenstone belts of Dharwar craton.

5.2.1 Petrography

Different fabric of the basement granitoids related to the different phases of deformation has been described in the previous chapter. The studied granitoids are mainly massive, but pockets of granitic gneiss occur in few places. Some of the rocks show evidence of intensive shear-related deformation. Granitoids are also subjected to intense fracturing. The modal composition of the samples is presented in Table 5.2.

The massive variety of the granitoids are leuco- to mesocratic, equigranular, coarse to medium grained rock consist of quartz, orthoclase, microcline, plagioclase (albite – oligoclase), and perthite with secondary minerals like biotite, chlorite and muscovite, and accessory phases like apatite, zircon, monazite, sphene showing hypidiomorphic granular texture (Fig. 5.2a). Ore bearing minerals are discussed in detail in the Chapter 6. Orthoclase and microcline (Fig. 5.2b) occur as plates and patchy grains. Microcline appears to be of two types – perthite type and interstitial platy type (Fig. 5.2c). Patchy and string perthite are very common and they do not show uniformity in distribution. Plagioclase occurs as subhedral and anhedral grains. Wart-like myrmekitic intergrowth (intergrowth of vermicular quartz and plagioclase) is observed along the microcline grain boundary (Fig. 5.2d). In some area, massive granitoids shows the porphyritic character where phenocrysts are represented by altered feldspar (Fig. 5.2e). Zoning presents within feldspar (Fig. 5.2f). Quartz-feldspar or K-feldspar-Na feldspar intergrowths are also a common feature. Biotite varies in colour from light brown to green (Fig. 5.2g) and locally occur as inclusions within K-feldspar (Fig. 5.2h). In places, biotite is associated with rutile, monazite and apatite where monazite occurs along the grain boundaries and fractures in apatite.

A primary incipient foliation presents in some pockets within the granitoids which is related to previously mentioned D1 and D2 deformation phase. The gneissic layering is marked by alternate quartzo-feldspathic and mafic bands where mafic bands are represented by mainly biotite and lesser amount of muscovite (Fig. 5.2i). Bending and kinking of biotite flakes is a

common feature within microfold (Fig. 5.2j). Dynamic recrystallization of quartz by bulging and subgrain rotation is very common while feldspar show wavy extinction.

Locally, gneissic fabric changes to strongly sheared, mylonitic fabric in the vicinity of outcrop-scale shear zones or to highly fractured varieties close to mesoscopic fault planes. The mylonitic foliation which is related to the D3 deformation phase mainly defined by parallel alignment of ribbon quartz alternating with very fine-grained quartz- feldspar-biotite rich matrix wrapping feldspar porphyroclasts (Fig. 5.2j). Feldspar porphyroclasts show elongation and marginal recrystallization along their boundaries (Fig. 5.2k). Development of asymmetric recrystallized grain-tail complexes against feldspar augen indicates both dextral and sinistral shear movements on mylonitic foliation planes (Fig. 5.2l). Twin lamellae in plagioclase grains show bending and kinking (Fig. 5.2e). Recrystallization of quartz and feldspar occur within such kink zones in large perthite.

Intense fracturing related to two deformational phases, i.e. D4 and D5 are well preserved in the microscopic scale (Fig. 5.2m). Intragranular to transgranular fractures cut across all the earlier planes. The gneissic foliation (S1 and S2) and mylonitic foliation (S3) get displaced by the fractures of varying orientation (Fig. 5.2n). The intra- to inter-granular fractures get connected with each other which lead to form cataclasite (Fig. 5.2o). The fractured horizons grade to zones marked by development of widespread brecciation, making a sharp contact with the host rock (Fig. 5.2p). Extensive alteration of host granite is observed in such

zones. Altered granitoids include chloritization (after biotite) (Fig. 5.2q), and sericitization (after plagioclase) (Fig. 5.2r). Epidote occurs both as veins and as discrete grains (Fig. 5.2s). These veins cut through the other minerals and appear to be younger than the other minerals within basement granitoids.

5.2.2 Geochemical data

Geochemical data often help in understanding the protolith history, mineralogical affinity and probable tectonic setting for an igneous rock suite. Major, trace and rare Earth element (REE) geochemistry of the granites has been carried out to understand the evolutionary history of the Chitrial area.

5.2.2.1 Major element data

Twenty-eight samples of granite were analysed for major element compositions. The results are presented in Table 5.3. Data reduction, recalculation and representation were done using the GCD-kit (Janoušek *et al*., 2006).

All the samples show SiO_2 variation (72.24–78.97 wt.%, Table 4.3) and are characterized by high K_2O (4.18 –7.31 wt.%) contents. Following the classification of Miyshiro, (1974), all the sample shows calc-alkaline nature within SiO_2 - FeOt/MgO variation diagram (Fig. 5.3a). Although the samples plot in the granite field in the normative Ab-An-Or diagram (Fig. 5.3b), they plot in the monzogranite field in the QAP diagram (Fig. 5.3c), but the sample CT31, plots within the alkali feldspar-granite field. K_2O vs. SiO_2 plot (Peccerillo and Taylor, 1976) suggests that all the samples belong to high-K calc-alkaline to

shoshonite series (Fig. 5.3d). They show peraluminous character with A/CNK values 1.0-1.6. This is also vindicated by their plots within the granite tectonic discrimination diagram of Frost *et al*. (2001) (Fig. 5.3e) and molar Na_2O – Al_2O_3 – K_2O plot (Fig. 5.3f). All the samples (Table 5.2) show high normative orthoclase (26-30%), while the sample CT 31 shows a maximum of 43%. Normative albite is low to moderate in all samples (22-30 %) while the sample CT 31 shows negligible value (~1 %). Normative anorthite is low in samples CT62F, CT65, CT31 and CT 210 (0.24-2.7%) moderate in samples CT207A, CT220, and CT206 (5.7-7.4%). The Harker (1909) plots show mostly linear trends with negative slope (TiO_2, FeOt, MgO, P_2O_5, Na_2O, CaO, Al_2O_3,) whereas K_2O does not display any significant variation with silica (Fig. 5.3g). The CaO/Na_2O ratio can be used to highlight the effect of source composition on granitic melts. For highly peraluminous granites with clay-rich sources, the CaO/Na_2O ratio is a valuable index of source composition and all the studied samples show distinctly lower values (0.10–0.48). Plot of all the samples within the fields II and III of A-B diagram (Debon and Le Fort 1983; Fig. 5.3h) matches with mineralogy which shows that biotite content is much higher than muscovite in all samples excepting one (sample CT31). This also validates the peraluminous nature of the samples. ACF diagram (El Baghdadi *et al*., 2003) indicates the S-type nature of the granites (Fig. 5.3i). Moreover, the plots of alkali, lime and ferromagnesian components (Patino Douce and Johnston, 1998) define coherent trends favouring low pressure crystallization of the magma (Fig. 5.3j).

5.2.2.2 Trace element data & REE data

Seven samples of granite were analyzed for major, trace and rare Earth element compositions. The results are presented in Table 5.4. Data reduction, recalculation and representation were done using the GCD-kit (Janoušek *et al*., 2006).

In terms of trace element composition, these samples represent more or less similar character with variable contents of Sr (22 – 276 ppm) and Ba (222 – 974 ppm). Samples CT31, CT62F and CT65 have low Sr (22-50 ppm), while sample CT206 have moderate Sr (97-152 ppm) and sample CT220 have high Sr (214-277 ppm) contents. Samples CT207A, CT62F and CT210 have low Ba (222-340 ppm), whereas samples CT65 and CT206 have moderate Ba (439-552 ppm) and CT220 contains very high Ba (974 ppm). Zr concentration is moderate in all the samples (146-249 ppm). All the samples contain moderate Rb and Y with high La/Nb (3.59-6.71) and low Ce/Pb (1.21-2.81) ratios. Zr, Cr, Sr, Y, Ba show negative linear correlation with SiO_2 whereas elements like Ni, Ce, and La do not display any such correlation. Rb shows a linear positive correlation with SiO_2 (Fig. 5.4a). According to the classification of Cabanis and Lecolle, (1989), all the granites show an affinity towards orogenic granite spatially related to active margin to post orogenic intracontinental domain (Fig. 5.4b). Classification and discrimination analysis were done using minor and trace elements like Ti, Zr, Y, Nb, Ga and Sc which remain relatively immobile during secondary alteration processes (Pearce, 1975; Ferrara *et al*., 1976). Plots of Zr vs. Ga/Al, FeOt vs. Ga/Al, Y vs. Ga/Al, Zn vs. Ga/Al, and Zn vs. Ga/Al show that the samples plot

under I, S and M - type fields (Whalen, 1987) (Fig. 5.4c). Tectonic discrimination diagrams with Rb vs. (Y+Nb), Nb vs. Y, Rb vs. (Ta+Yb) and Ta vs. Yb show that all the samples plot in the boundary between syn-collisional and volcanic arc granites, except sample CT65 which plots close to the boundary of syn-collisional, volcanic arc and within-plate granites (Pearce *et al*., 1984; Fig. 5.4d).

Seven samples of granite were analyzed for rare Earth element compositions. Selected large ion lithophile element and high field strength element ratios (e.g. Rb/Nb, Th/Ta, La/Ta, Rb/Zr) can be used as indicators for potential crustal source reservoirs. It is thought that these ratios can remain unchanged, or are enriched, in melts produced from anatexis. The results are presented in Table 5.4. Chondrite normalized REE patterns (Boynton, 1984) are distinctly more enriched and fractionated for LREE than for HREE and commonly exhibit negative Eu anomalies (Eu/Eu*=0.35 – 0.88) (Fig. 5.4e). All the samples are Sr-poor, and low to moderate Sr/Y (1.2 – 26.1) ratio indicates low – pressure melting condition of the source. Primordial mantle normalized plots show distinct enrichment of LILE (especially Rb, U, Th, La, and Ce) and prominent troughs at Ba, Sr, Nb, and P anomalies (Fig. 5.4f). Out of seven samples, only sample CT206 shows very low Eu anomaly (Eu/Eu*=0.88) and more depleted in HREE than other samples (∑REE=180.41) whereas other six samples represent more or less similar character with strong (Eu/Eu*=0.30-0.55) to moderate (Eu/Eu*=0.76) negative Eu anomalies. Samples CT210 and CT207A show moderate Eu anomaly (Eu/Eu*=0.55, 0.30) with moderately enriched LREE and less depleted HREE (∑REE=228.92, 394.81). Primordial mantle-normalized plots of sample CT210

and 207A are characterized by highly enriched Rb, Th, La and Nd, moderately depleted in Nb, Cs, Ba, less prominent troughs at Sr and prominent troughs at P. U enrichment is higher in sample CT210. Sample CT220 represents more enrichment in LREE and less depleted in HREE (∑REE=327.84) compared to other samples. It shows weak negative Eu anomaly (Eu/Eu*=0.76). Primordial mantle-normalized plot of sample CT220 is characterized by highly enriched Cs, Rb, La, Ce, Nd, moderately enriched in Th and U, less depleted in Ba, Sr moderately depleted in Ta, Nb, and prominent troughs at P. Samples CT31, CT65, CT62F, show less- enriched LREE pattern and moderately depleted HREE (∑REE=187.62, 161.27, 286.14) with highest Eu depletion (Eu/Eu*=0.35, 0.45, 0.37) compared to others. Primordial mantle-normalized plot of sample CT31 represents that the sample is highly enriched in U, moderately enriched in Th, Rb, Hf and Zr, moderately depleted in Ba,Ta, Nb, and prominent troughs at Sr and P, whereas primordial mantle normalized plot of CT65 shows that the sample is moderately enriched in U, Th, Rb, Nd, no anomaly in Ta, Nb, La, Ce moderately depleted in Ba, Sr, and prominent troughs at P. Primordial mantle normalized plot of CT62F is characterized by highly enriched Th, and Ta, moderately enriched in Nd, La, Ce, U, moderately depleted in Nb, Cs, Ba and prominent troughs at Sr and P. Many HREE and Y have high partition coefficients and high Gd/LuN ratio (Gd/LuN= 1.2 to 1.6 there is little or no depletion in these elements.

5.2.2.3 Geothermometry using zircon shape and saturation temperature

The estimation of melting temperatures of granitic melts is often based on conventional saturation thermometers (Watson, 1979; Watson and Harrison, 1983; Montel, 1993). However, in granitic rocks with abundant inherited zircon, the zircon saturation temperatures can be used as common thermometer for the melt (Miller *et al*., 2003).

On the basis of morphology and shape of zircon crystals, two morphological types of zircon (Pupin, 1980) were recognized from the granite. Type 1 zircons (Fig. 5.5a) show a well-developed {110} prism and two pyramids, {101} and {211}, with the latter more dominant. They belong to subtypes S12, S17 and of S21 Pupin's typological classification (Fig. 5.5). Type 2 zircons (Fig. 5.5b) have a well-developed {100} prism and two pyramids, {101} and {211}, with the pyramid {101} more dominant. They correspond to subtypes S18, S19, S20 of Pupin's typological classification (Fig. 5.5). Based on the morphology of zircon crystal (Fig. 5.5), the temperature of formation of zircons in Chitrial granite is in the range of 750° to 800°C.

Temperature calculation method based on degree of zircon saturation

Watson and Harrison (1983) provided the following equation between zircon solubility, temperature and magma composition:

$$\ln D^{Zr,\ Zircon/melt} = \{-3.80 - [0.85\ (M-1)]\} + 12900/T\ [K]$$

$$T_{Zr} = 12900/\ [2.95 + 0.85M + \ln (496000/Zr_{melt})]$$

In this equation $D^{Zr,\ Zircon/melt}$ is the ratio of zirconium concentration in zircon (ppm) mineral to the zirconium concentration in the magma. The number 496000 is the concentration of Zr in ppm, and T represents the temperature in Kelvin. Also, M is a cation ratio that depends on the solubility ratio of zircon to SiO_2 as well as peraluminous nature of magma, which is calculated using the formula below:

$$M = (Na + K + 2.Ca)/ (Al.Si)$$

As shown in Table 5.5, the crystallization temperatures of zircon of studied samples have been calculated as 772-792°C. These values are in line with those obtained during studying zircons from morphological standpoint (750-800°C).

5.2.3 Petrogenesis of granitoid

Major element data of twenty eight samples and trace and REE data of seven samples of the Chitrial granite suite show geochemical signatures with high and restricted SiO_2 range (72.24–78.97 wt.%) and are characterized by high K_2O (4.18 –7.31 wt%) content. All the samples are Sr-poor, and low to moderate Sr/Y (1.2 – 26.1) ratio indicates low-pressure melting condition of the source (Bickle *et al*., 1989).

All the granite samples of the Chitrial area plot within I, S and M - type granite fields according to the diagram of Whalen, (1987) (Fig. 5.4c). Although the alphabetical classification of granites (I-, S-, A-, M- and C-types) is popular in use, there are controversies on the assumptions and applicability of such simple

classification scheme (discussed in Frost *et al*., 2001; Chappell and White, 2001). It was originally proposed that the I-type granites are metaluminous to weakly peraluminous, relatively sodic in character with wide range of silica (56-77 wt.%) and inferred to have originated from a mafic, meta-igneous source (Chappell and White, 1974). The S-type granite, on the other hand, shows strongly peraluminous, relatively potassic character with higher range of silica (64-77 wt.%) and interpreted to have formed from partial melting of sedimentary rocks (Chappell and White, 1974). This classification scheme considers that granites have simple sources which can be interpreted only from geochemistry, but it has been proven wrong as the source of granite could be complex with components from both mantle and crust (John and Wooden, 1990; Miller *et al*., 1990; Collins, 1996). Despite limitations, distinction between I-type and S-type granites could be made based on field relationships, such as presence of metasedimentary xenoliths within S-type granite in contrast to hornblende-bearing enclaves in I-type (Chappell and White, 2001). Petrographic features can also help in identifying the nature of source as hornblende is common in the more mafic I-type granites, whereas muscovite and biotite are common in more felsic S-type granites. Sphene is a common accessory in the I-type granites whereas monazite commonly occurs in S-type granites (Chappell and White, 2001). The I- and S- type granites were further augmented by the introduction of A-type granites (Loiselle and Wones, 1979) that is relatively potassic, has high FeO/(FeO+MgO) and has high Zr. The latter are rarely deformed, emplaced well after the youngest orogenic event, and hence termed anorogenic (A-type).

The Chitrial granites contain dominantly biotite- and muscovite-rich microgranular metasedimentary enclaves (Fig. 3.3h, i). Other chemical signatures like the ratio of mol. Al_2O_3/ (K_2O+ Na_2O+CaO) (Chappell and White, 2001) also indicate S-type character (>1.1 as in Table 5.2). These rocks show normative corundum (0.83-2.12 %), peraluminous chemistry and presence of both biotite and muscovite; all indicative of highly felsic S-type character. Rb/(Y+Nb) and Nb/Y plots indicate syn-collisional to volcanic arc tectonic setting, characteristics of orogenic S-type granites (Pearce *et al*., 1984; Fig. 5.4d). Texturally, the granites grade from massive to highly foliated varieties indicating their heterogeneous deformation character. So, all the evidences converge towards the fact that Chitrial granite suite is compositionally S-type and is syn-tectonic in nature. Interestingly, Verma *et al*. (2008) described A-type character from the Chitrial granite suite. However, it has been amply demonstrated in the present study that as per field, petrographic and deformational characteristics, the Chitrial granite suite could be reasonably equated with S-type granites. The main basis of A-type classification by Verma *et al*. (2008) was on trace element plots (see Figs. 13a-d of Verma *et al*., 2008). On the contrary, our trace element plots clearly show that the granites fall in the S-type field. A comparison could not be drawn with Verma *et al*. (2008) since trace element data were not provided in that study. High La/Nb and low Ce/Pb ratios and negative Nb anomalies of all the samples are characteristics of convergent margin magmas (Rudnick, 1995). The Nb-anomaly is probably inherited from the magma source, and possibly reflects a subduction-related geochemical signature of the source (El Baghdadi *et al*., 2003).

This indicates a trace of I-type component (TTG type) of granite magma in the Chitrial area which is expected in a subduction-related setting as documented from the South Morocco (El Baghdadi *et al*., 2003). El Baghdadi *et al*. (2003) also reported A-type granite from the same suite which was emplaced during the post-subduction rifting. It is thus possible that the A-type granite reported by Verma *et al*., (2008) was formed in a similar setting within the larger Chitrial granitic suite. Negative Sr anomaly possibly implies plagioclase fractionation. The absence of Eu anomaly in sample CT206 could be related to absence and/or the destabilization of plagioclase at the source region (Johnson *et al*., 2003). Therefore, the evolved geochemical composition resembles the granite composition produced by typical intracrustal melting of Archaean sediments (Beakhouse and McNutt, 1991; Bickle *et al*., 1989; Champion and Sheraton, 1997; Jahn *et al*., 1988; Moyen *et al*., 2003a; Subba Rao *et al*., 1998; Sylvester, 1994). Since the granites show broadly S-type characters, these could have been generated due to melting of metasediments of the middle crust (Kemp *et al*., 2007).

5.3 Geochemistry and provenance study of the Srisailam Formation

The basin contains quartzite/ pebbly quartzite/ grit at the base, followed by intercalation of dark grey overlie on the Archean granite basement**.** Srisailam sediments are represented by characteristic sequence of ferruginous quartzite followed subsequently by shale – siltstone, massive quartzite and quartzite – shale intercalations while basal part is marked by presence of gritty quartzite. Soft

sedimentary (penecontemporaneous) deformational structures like overturned cross bedding, load structure, convolute bedding/laminations, are conspicuous in quartzite – shale and shale – siltstone intercalated sequences present near Nagarjun sagar.

5.3.1 Petrography

Srisailam quartzite is bimodal in mineral distribution and consists predominantly of microcrystalline and polycrystalline quartz with little amount of chert and alkali feldspar while secondary overgrown quartz and minor calcite are the cementing materials. Tourmaline, zircon and monazite are found as heavy minerals. The cover rocks are composed of sandstones and less common siltstone and shale. The analyzed sandstone samples of the Srisailam Formation are medium- to coarse-grained, subangular to subrounded, and moderately to poorly sorted (Table 5.1). All types of major grain contact, including float, point, long, and concave –convex, are present. However, an abundance of point contact was noted (Fig. 5.6a). Sandstone classification was made using the Dott–McBride scheme. The Srisailam sandstones are mostly quartz arenites with subordinate sublithic arenites and have an average framework composition of Q – 92.07; F – 0.31; R – 7.62. The framework grains are mainly quartz (69.54% of the rock volume) and less frequently of feldspar, rock fragments, and heavy minerals (avg. 6.15%). Framework constituents account for 86% of the rock, and the matrix and cement constitute about 14%. The matrix partly consists of clay minerals and detrital constituents. The observed types of cement include mainly silica (Table

5.6). Average existing pore space constitutes 7.84% of the rock. Quartz and feldspar are the most abundant framework grain in the sandstones, constituting an average 95.07% of rock volume. Quartz grains are commonly subangular to subrounded in shape (Fig. 5.6b). Most of the quartz grains show multiple deformation fractures (Fig. 5.6c and 5.6d). Among quartz grains, Qm (95.9 vol.%) is dominant over Qp. Most of the Qm grains have undulatory extinction. Some of quartz grains contain inclusions of rutile, zircon, and tourmaline (Fig. 5.6e). Long, point, and concavo-convex contacts are common and are caused by pressure solution and compaction. Some quartz grains display syntaxial overgrowths (Fig. 5.6f), and some others are corroded at their margins (Fig. 5.6g). Heavy minerals, mica flakes and clay minerals (kaolinite, illite, mixed clay, and chlorite) also exist. Mica and heavy minerals (rutile, zircon, and tourmaline) appear in accessory quantities (<1.0%; Table 5.6). Feldspars in the quartzite are illitised and such alteration is more pronounced in plagioclase feldspars (Fig. 5.6h). Feldspars are mostly subangular and clear of inclusions. Orthoclase, microcline, and perthite are the most common varieties. K-feldspar (K) (avg. 0.45%) dominates over plagioclase (avg. 0.20%) and is mostly orthoclase and microperthite, with fewer microcline grains. Most feldspar grains are altered, which implies a high degree of chemical weathering.

5.3.2 Geochemical data

5.3.2.1 Major element data

Major element geochemistry gives an idea about the provenance type as well as weathering conditions which in turn are controlled by the tectonic setting of the basin. Major oxides compositions (wt %) of 8 samples of the Chitrial sandstones are presented in Table 5.7. In the analyzed samples, concentrations of major elements vary narrowly. The sandstones consist of SiO_2 mainly. Total iron is expressed as Fe_2O_3.

The studied clastic sediments, comparable to quartz arenites of Pettijohn (1975) have SiO_2 content varying from 84-98 wt% with Al_2O_3 (1.95 – 8.87 wt%) concentrations TiO_2 contents of about 0.01 wt% and Fe_2O_3+MgO content of 0.54 wt%. High SiO_2 content reflects the quartz-rich nature of the studied sandstones and high SiO_2/Al_2O_3 ratio >10 (Chemical maturity index, average 13.69), indicate high chemical maturity of the investigated samples. Compared to the average sandstone composition proposed by Turekian and Wedepohl (1961), the studied samples are depleted in CaO, Al_2O_3, Fe_2O_3 and Na_2O and relatively high K_2O (average 2.778 wt.%) (Table 5.7). Depletion of Na_2O (<1 wt %), relative enrichment of K_2O content and the significantly higher K_2O/Na_2O ratios may be due to significantly higher concentration of K-feldspar. K_2O and Na_2O contents and their ratios (K_2O/Na_2O >1) are also consistent with the petrographic observations, which shows K-feldspar dominates over plagioclase feldspar. It has also been noticed that all the Chitrial sandstones are not plotted in the typical fields but near the log Na_2O/K_2O line (below -1.0 line). In the geochemical

classification diagram of Herron (1988), the analyzed Chitrial sandstones plot in quartz arenite (Fig. 5.7a). Binary variation diagrams of SiO_2 versus Al_2O_3, Fe_2O_3, and K_2O of all the analyzed samples display negative linear trends (Fig. 5.7b). While binary variation diagrams of Al_2O_3 versus K_2O and Fe_2O_3 of all the analyzed samples display positive linear trends (Fig. 5.7c). The ratio of SiO_2/Al_2O_3 against that of quartz and chert / (feldspar + rock fragments), (Q/F+RF) was plotted (Fig. 5.7d) which is interpreted to reflect the maturity of sandstones (Pettijohn 1975). Higher SiO_2 ratio coincides with higher silica phases of quartz, quartzite and chert, which in turn, reflects that such sandstones are mature. A bivariant plot of SiO_2 against total $Al_2O_3+K_2O+ Na_2O$ (Suttner and Dutta, 1986) was used in order to identify the maturity of the studied samples (Fig. 5.7e). It indicates the semi-arid to semi-humid climatic conditions for the samples investigated. Modal analyses of framework components of studied sandstone samples (Table 5.5) have been plotted on the Qt-F-L ternary diagram (Fig. 5.7f) of Dickinson *et al*. (1983) which indicate the studied sandstones as recycled orogenic product. According to Roser and Korsch (1988), unstandardized discriminant function scores of the samples (F1 and F2) for major elements were plotted following the boundaries between fields (P1-P4). The studied samples plot within the P4 field (Fig. 5.7g). According to F1 – F2 diagram (Bhatia, 1983) the samples show a affinity of passive margin field (Fig. 5.8a). Samples also show the same affinity when it is plotted in the K_2O/Na_2O vs. SiO_2 (Roser and Korsch, 1988) diagram (Fig. 5.8b). The discriminant function diagram

using major element (Roser and Korsch, 1988) shows all the samples plotted in the felsic igneous source.

5.3.2.2 Trace element and REE data

Trace element concentrations of 5 samples of the sandstones are provided in Table 5.8. In the Chitrial sandstones, the contents of large ion lithophile elements (LILE) like Rb, Ba, Sr and Th vary from 13 to 177 ppm, 37 to 219 ppm, 5 to 17 ppm and 1 to 4 ppm, respectively. The concentrations of high field strength elements (HFSE) like Zr, Y and Nb range from 16 to 38 ppm, 1 to 3 ppm and 0.5 to 1.6 ppm, respectively. Similarly, transition trace elements (TTE) like V, Cr, Ni and Zn range from 7 to 10 ppm, 58 to 74 ppm, 10 to 22 ppm, and 18 to 46 ppm respectively. Co varies from 4.88 to 9.55 ppm; Cu from 12 to 28 ppm. Cr shows positive correlations with Ni (r = 0.32) and Zn (r = 0.38). Ni shows positive correlations with Co (r = 0.26) and Cu (r = 0.14). The sandstones have low contents of Cr (average = 68 ppm) and Ni (average = 14 ppm). Cr/Ni ratios vary from 3.27 to 6.4 ppm (average = 5.12 ppm). Sc-V plot shows a decrease in the abundances of both Scandium and Vanadium (Fig. 5.8b). There are distinct negative anomalies in Rubidium (Rb), Niobium (Nb), Tantalum (Ta), and Barium (Ba). Ba/La and Eu/Eu* values are greater than 1. In comparison with average upper continental crust (UCC), the concentrations of most trace elements are generally low with exception of Co that is consistently enriched relative to upper continental crust for all the analysed samples. The average Th/U ratio in the

samples is 4.13 ppm whereas La/Th ratio varies between 1.6 and 2.7. Th/Sc, Th/Co ratios are appreciably high.

The REE abundance and the distribution pattern of the analytical data are useful in understanding the petrogenesis of different types of arenites (Bhatia, 1985; Bhatia and Crook, 1986; McLennan, 1989; Condie, 1991; McLennan and Taylor, 1991). REEs are among the most important group of elements in terms of provenance indicator. These REE diagrams compare the rare Earth element (REE) concentrations normalized to the C1 chondrite values of Sun and McDonough, (1989). Concentrations are also normalized to Lu which indicates a strongly enriched in the light rare Earth elements (REE) and have relatively modest middle to heavy-REE slopes (Fig. 5.8e). Large negative Europium (Eu) anomalies are common (McLennan *et al*., 1993) without the pronounced flattening. Upper Continental Crust Spider diagrams compare the samples from this study to the average Upper Continental Crust of Taylor and McLennan (1995) (Fig. 5.8f). Sediments are characterized by relatively flat to slightly LREE-enriched patterns with small positive Eu anomalies. The LREE/HREE, La/Sc, Th/Sc, Th/Co ratios are appreciably high. The La_n/Yb_n and La/Th ratios vary between 9 to 35 and 2.07 to 9.27 respectively.

5.3.3 Petrogenesis of Srisailam Formation

The studied clastic sediments, comparable to quartz arenites of Pettijohn et al., (1972), have SiO_2 content varying from 90-97 wt% with TiO_2 concentrations averaging 0.01 wt%, Al_2O_3 contents of about 3.65 wt% and Fe_2O_3+MgO content

of 0.22 wt%. Compared to the average sandstone composition proposed by Turekian and Wedepohl (1961), the studied samples are depleted in CaO, Al_2O_3, Fe_2O_3 and Na_2O (Table 5.6). The negative correlation of SiO_2 with most major elements is due to most of the silica being secreted in quartz (Turekian and Wedepohl 1961). Depletion of Na_2O is attributed to the relatively small amount of Na-rich plagioclase present.

Selected trace elements such as La, Ce, Nd, Y, Th, Zr, Hf, Nb, Sc, Co and Ti are useful in discriminating provenance and tectonic setting of sedimentary basins because of their relative immobility during sedimentary processes (Bhatia and Crook, 1986; Rollinson, 1993). In comparison with average upper continental crust (UCC), the concentrations of most trace elements are generally low with exception of Co that is consistently enriched relative to UCC for all the analyzed samples. Cr/Ni ratios vary from 3.27 to 6.4 ppm (average = 5.12 ppm) which features indicate that Cr and Ni constitute components of clay minerals and other detrital material (e.g., chlorite, ferromagnesian minerals) (McCann, 1991). The passive margin setting plays an important role for the formation of the studied sandstone which is vindicated by F1 – F2 diagram of Bhatia, 1983 (Fig. 5.8a) and Sc – V trace element diagram (Fig. 5.8d). Large negative Europium (Eu) anomalies are common (McLennan *et al*., 1993) without the pronounced flattening seen in other cratonic sediments indicating mechanical fractionation of plagioclase out of the system during weathering and transport. Sediments are characterized by relatively flat to slightly LREE-enriched patterns with small positive Eu anomalies that reflect the small negative anomaly characteristic of

upper continental crust. It is also indicating a passive margin set up (Bhatia, 1985; McLennan *et al*., 1993).

5.3.4 Provenance of the Srisailam Formation

Several investigations have suggested that the chemical and mineralogical compositions of siliciclastic sedimentary rocks are related to those of their source and these compositions has been used to categorize the precursor rock from which the investigated sedimentary rocks were derived (e.g., Kalsbeek and Frei, 2010). The framework compositions of the siliciclastic sandstones are a reliable indicator of the tectonic setting and the provenance. The Qt-F-L ternary diagram of Dickinson et al., (1983) indicates the provenance of the Chitrial sandstone as a product of recycled orogen (Fig. 5.7f). The average value of Na_2O/Al_2O_3 ratio of the studied clastic sediments ranges between 0.09 and 0.37 (av. 0.24) which indicates that the sodic/tonalitic rocks were not predominant in the source region. The Low value of Cr in the studied clastic sediments is 35 ppm and low value of Ni is 1.75 ppm, which accounts for felsic provenance (Hayashi *et al*., 1997). The Zr/Y ratio of the studied clastic sediments ranges from 10-29 (average 16) which accounts for felsic source (Wrafter *et al*., 1989, Taylor and McLennan, 1985). According to Roser and Korsch (1988), to infer provenance, unstandardized discriminant function scores of the samples (Discriminant Function1 and Discriminant Function 2) were plotted within the field, which represents recycled quartzose sedimentary provenance (Fig. 5.7g). Recycled sources represent quartzose sediments of mature continental provenance and the derivation of the

sediments could be from a highly weathered granite / granite-gneiss terrain. On the basis of sedimentary geochemistry, the optimum discriminations of the tectonic settings of sedimentary basins have been previously achieved using major, rare earth and trace elements. The studied samples have low abundance of Fe_2O_3+MgO (av. 0.36-0.73 wt%) and TiO_2 (av. 0.065 wt.%) contents, higher Al_2O_3/(CaO+Na_2O) (2.39-10.34) ratios and K_2O/Na_2O (0.54-3.08) ratio with relatively lower Al_2O_3/SiO_2 (0.01-0.05) ratio, which indicate passive margin setting (Mader, and Neubauer, 2004; Roser et al., 2000; Girty *et al*., 1993). The K_2O/Na_2O-SiO_2 diagram (Roser and Korsch, 1986) (Fig. 5.8b) and Sc-V diagram (Fig. 5.8d) (Bhatia and Crook, 1986) also vindicated that all the studied samples are the product of passive margin setting. Moreover, in the D1 – D2 discrimination diagrams (Fig. 5.8c) after Roser and Korsch, 1988 indicate that the studied samples derived from the felsic igneous provenance. Furthermore, distinctly similar geochemical characteristics of the studied clastic sediments samples suggest that they were sourced from same provenance.

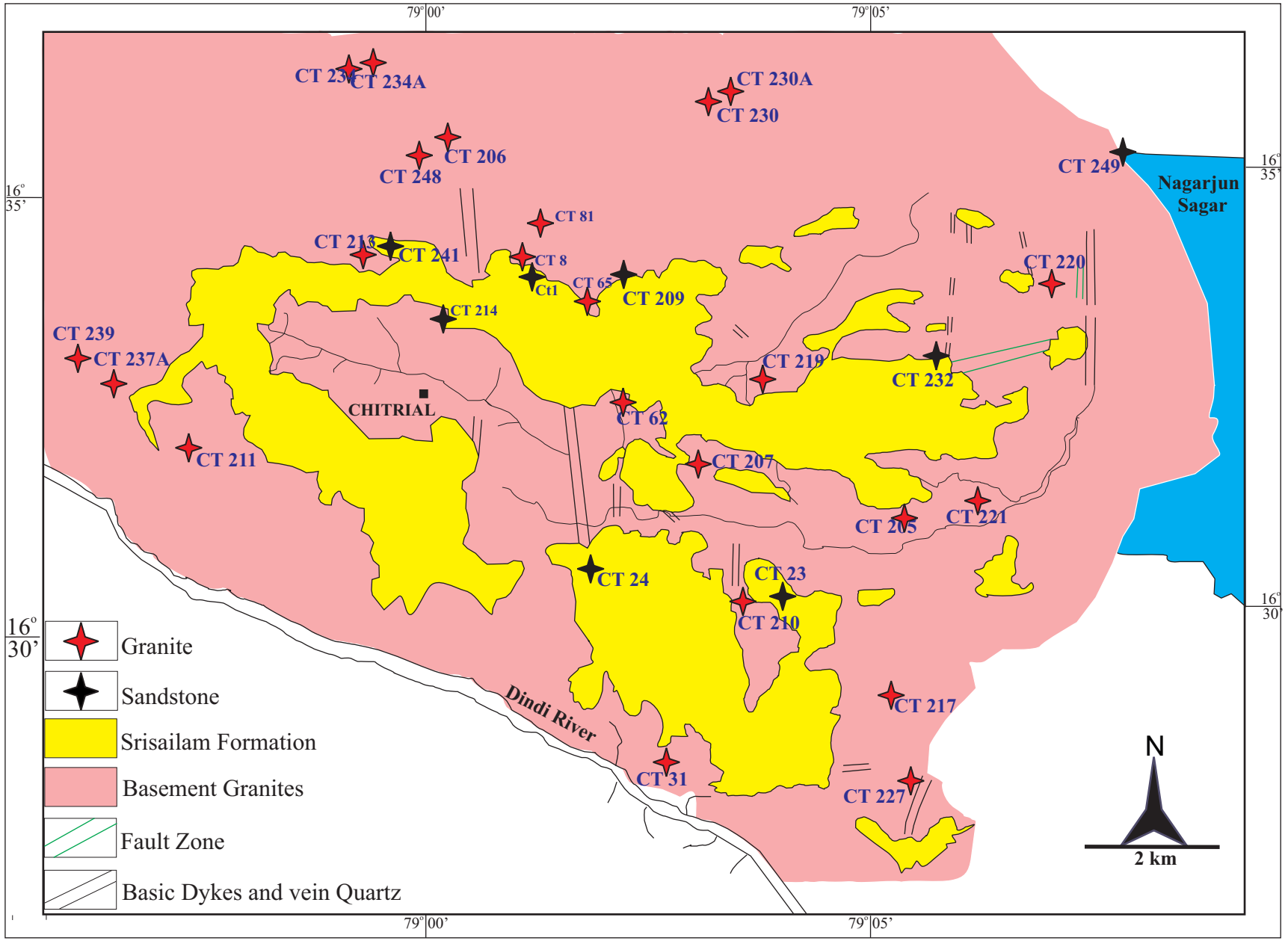

Figure 5.1: Geological map of the Chitrial Outlier, (modified after Verma et al., 2009) showing the sample location. Red star denotes the position of granite samples whereas black star represents the position of the sandstone samples.

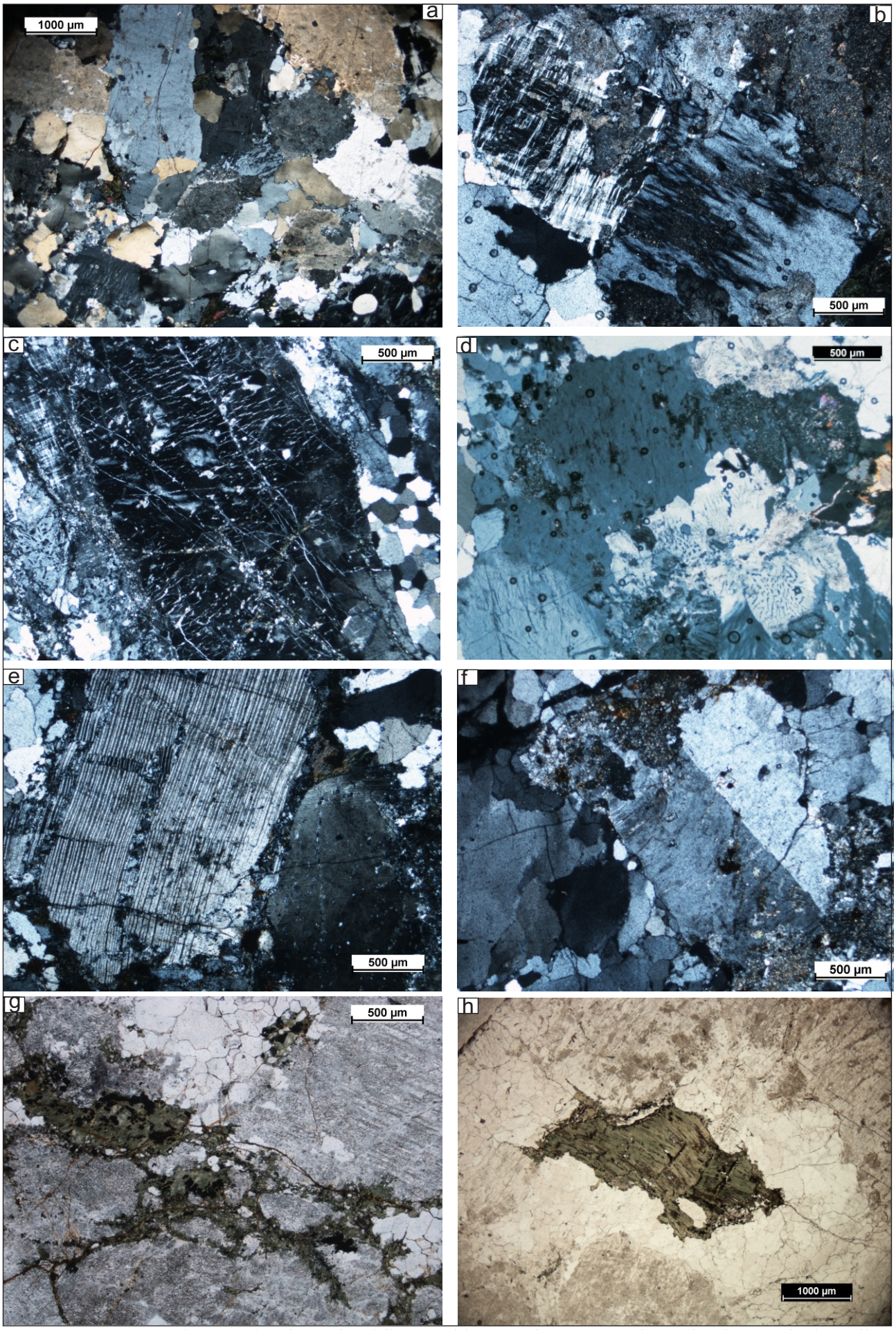

Figure 5.2: (a) Massive granite shows hypidiomorphic granular texture, (b) Orthoclase and microcline occur as plates and patchy grains within basement granitoid, (c) Perthite type and interstitial platy type microcline presents within basement, (d) Wart-like myrmekitic intergrowth presents along the microcline grain boundary, (e) In porphyritic granite twin lamellae in plagioclase phenocryst grains show bending and kinking, (f) Zoning presents within feldspar, (g) Light brown to green pleochroic biotite is very common, (h) Biotite occur as inclusions within K-feldspar.

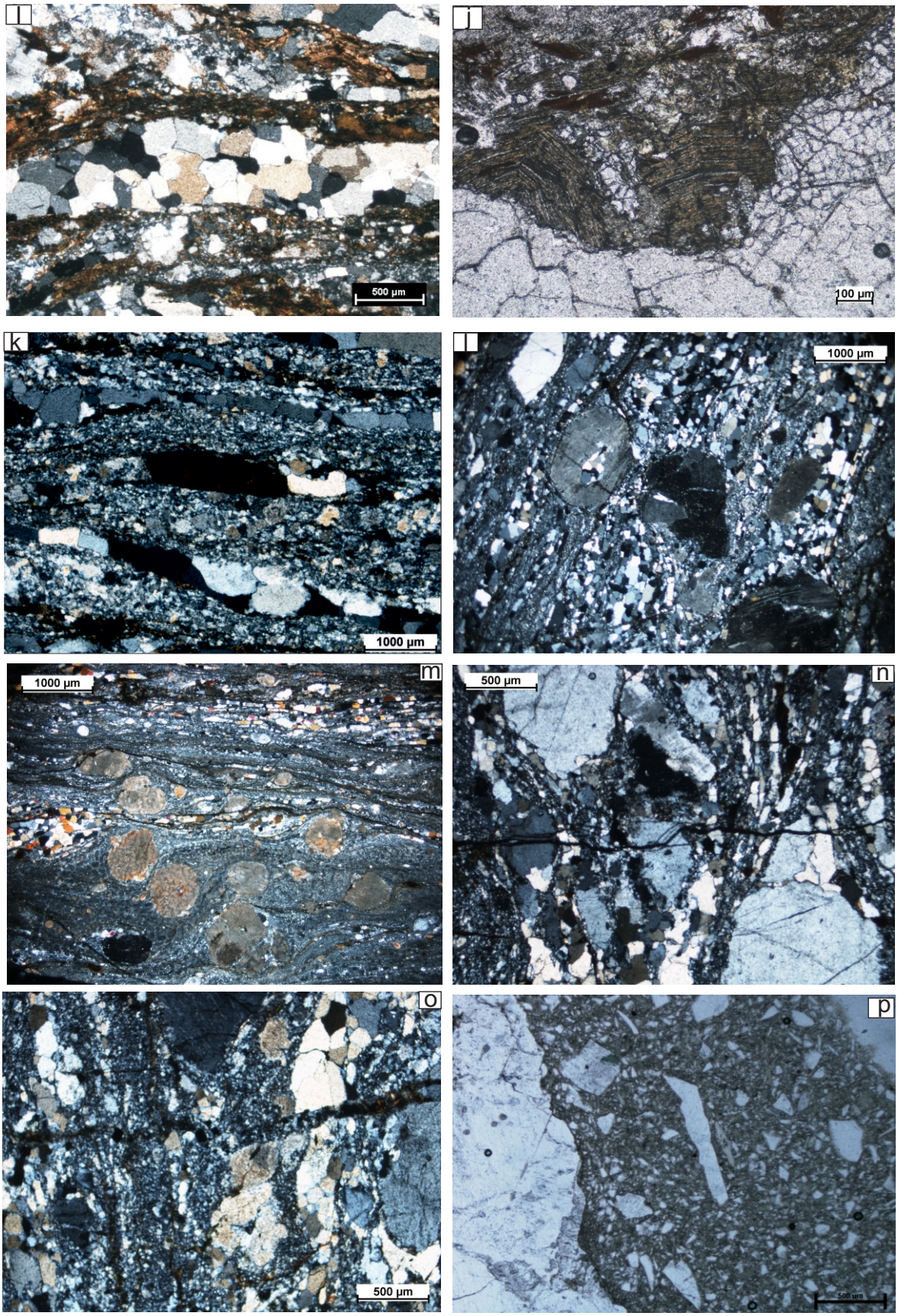

Figure 5.2: (i) The gneissic layering is marked by alternate quartzo-feldspathic and mafic bands where mafic bands are represented by mainly biotite and lesser amount of muscovite, (j) Bending and kinking of biotite flakes is a common feature (k) ribbon quartz alternating with very fine grained quartz- feldspar-biotite rich matrix wrapping feldspar porphyroclasts, (l) Feldspar porphyroclasts show elongation and marginal recrystallization, (m) Asymmetric recrystallized grain-tail complexes against feldspar augen indicates both dextral and sinistral shear movements on mylonitic foliation planes, (n) Intragranular to transgranular fractures presence within granitoid. (o) The gneissic foliation (S1 and S2) and mylonitic foliation (S3) get displaced by the fractures of varying orientation, (p) The intra- to inter-granular fractures get connected with each other which lead to form cataclasite.

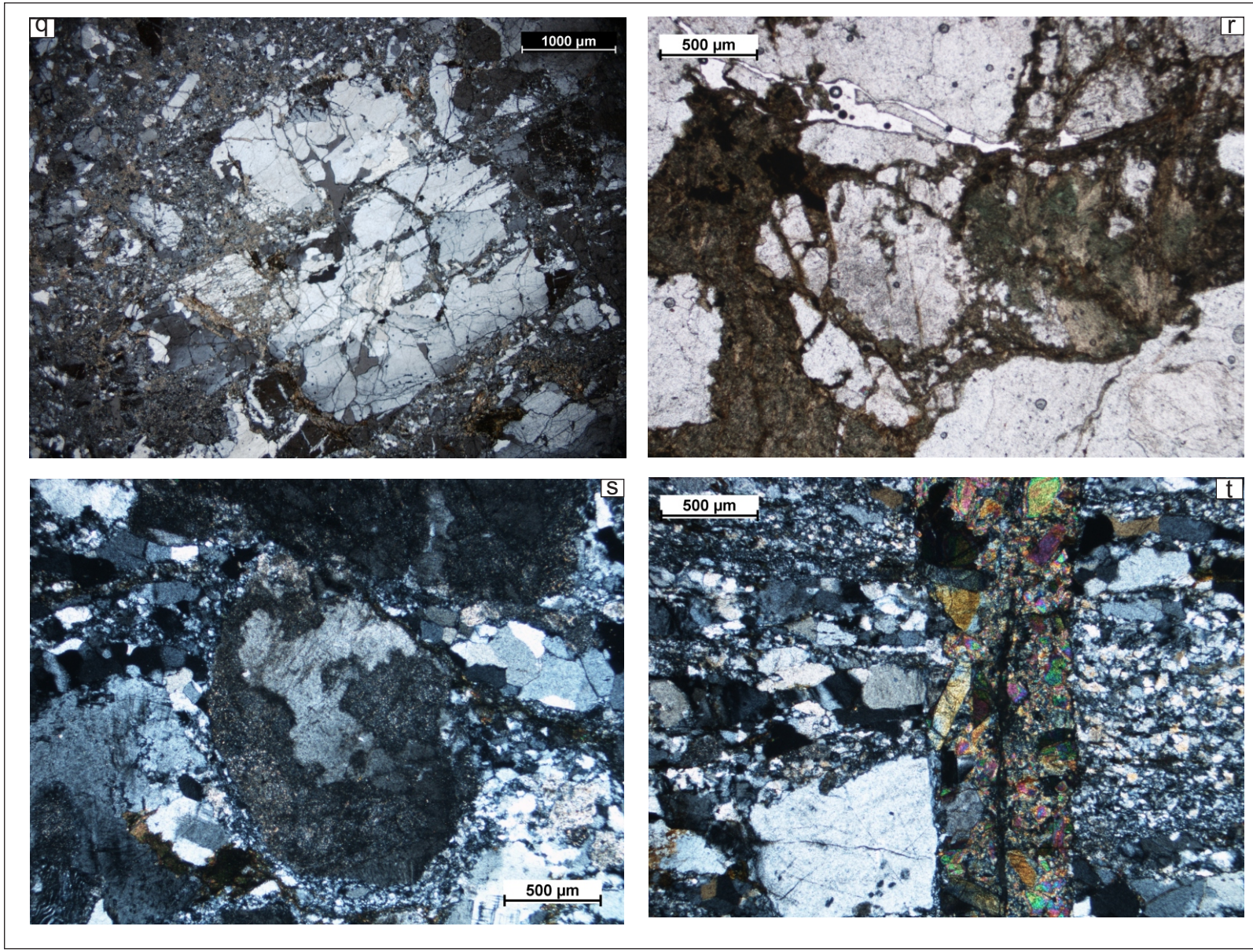

Figure 5.2: (q) Brecciation, making a sharp contact with the host rock, (r) Chloritization (after biotite) is very common, (s) sericitization (after plagioclase) is the main alteration product, (t) Epidote occurs both as veins and as discrete grains.

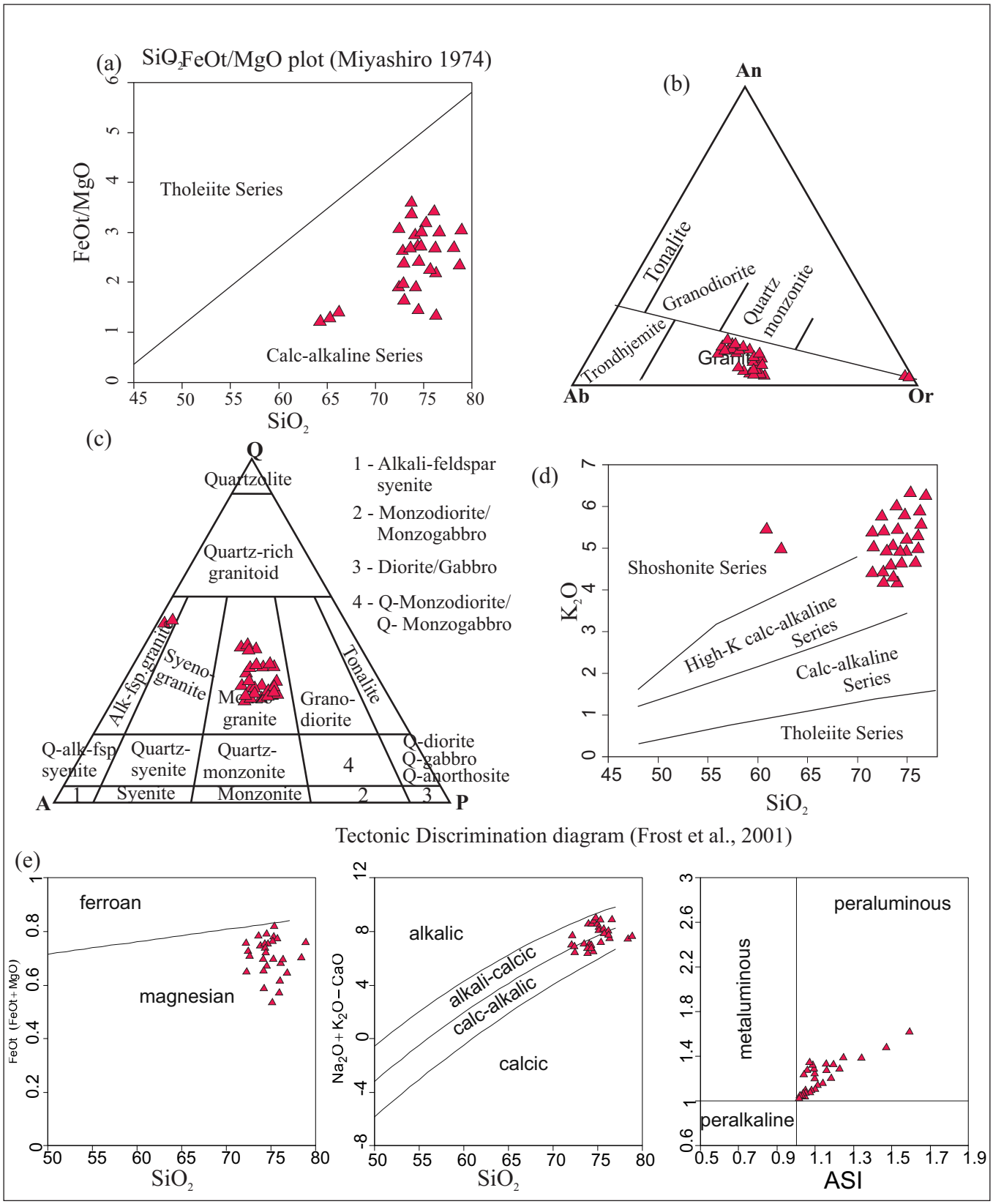

Figure 5.3: (a) Classification of Miyshiro (1974), shows all the sample plot in calc-alkaline series within SiO2 - FeOt/MgO variation diagram, (b) Feldspar composition triangle (O'Connor, 1965) showing plots of all the samples within the granite field. (c) QAPF diagram showing six samples plot within monzogranite field and one sample within the alkali-feldspar granite field. (d) SiO2-K2O plot (Peccerillo and Taylor, 1976) of all the samples showing high-K, calc-alkaline affinity. (e) Plot of all the samples within discrimination diagram (Frost et al., 2001) shows magnesian and peraluminous character.

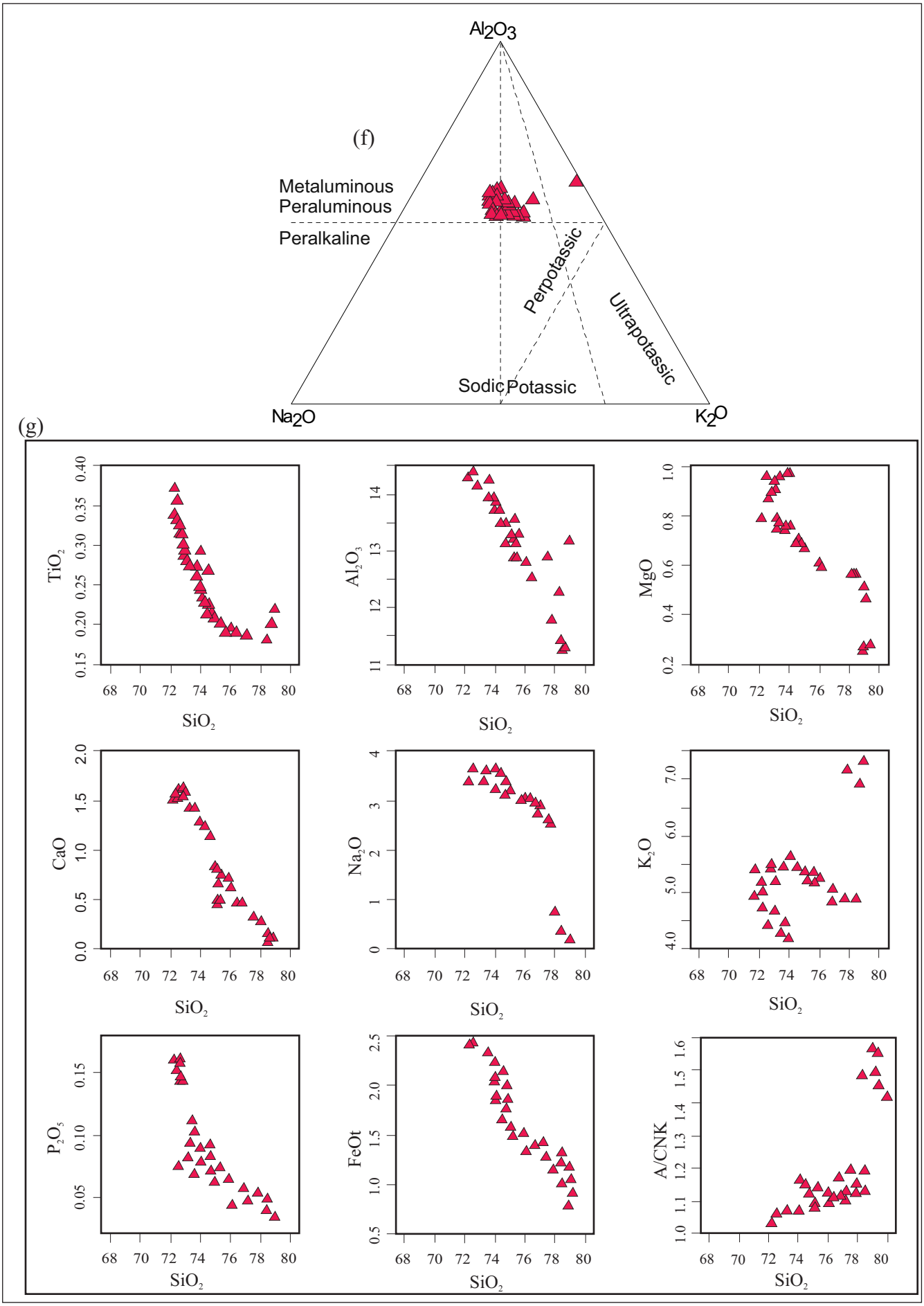

Figure 5.3: (f) Na2O – Al2O3 – K2O plot supports the paeraluminous character of the samples. (g) Harkar diagram shows the variation diagram of major oxide with SiO2.

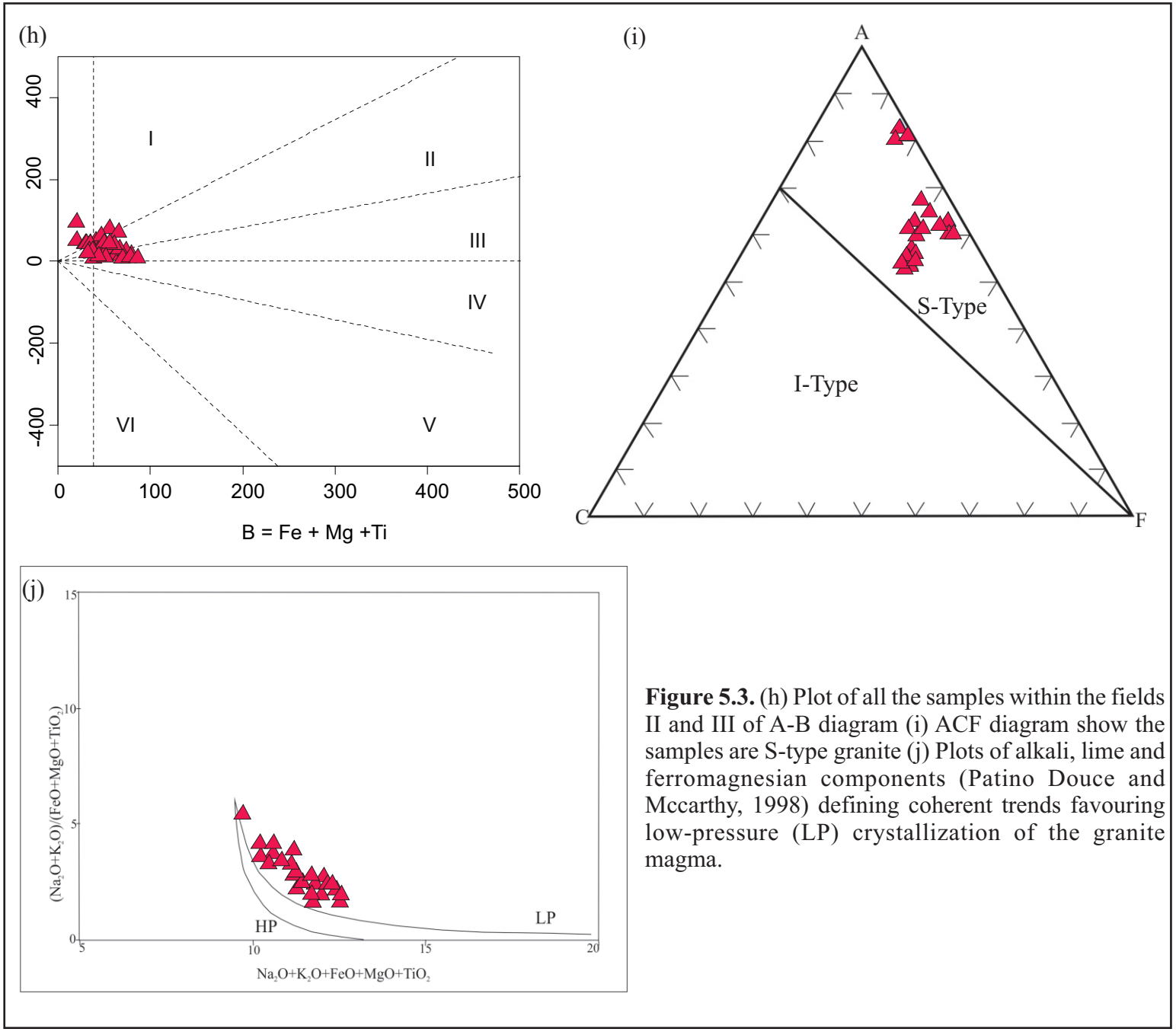

Figure 5.3. (h) Plot of all the samples within the fields II and III of A-B diagram (i) ACF diagram show the samples are S-type granite (j) Plots of alkali, lime and ferromagnesian components (Patino Douce and Mccarthy, 1998) defining coherent trends favouring low-pressure (LP) crystallization of the granite magma.

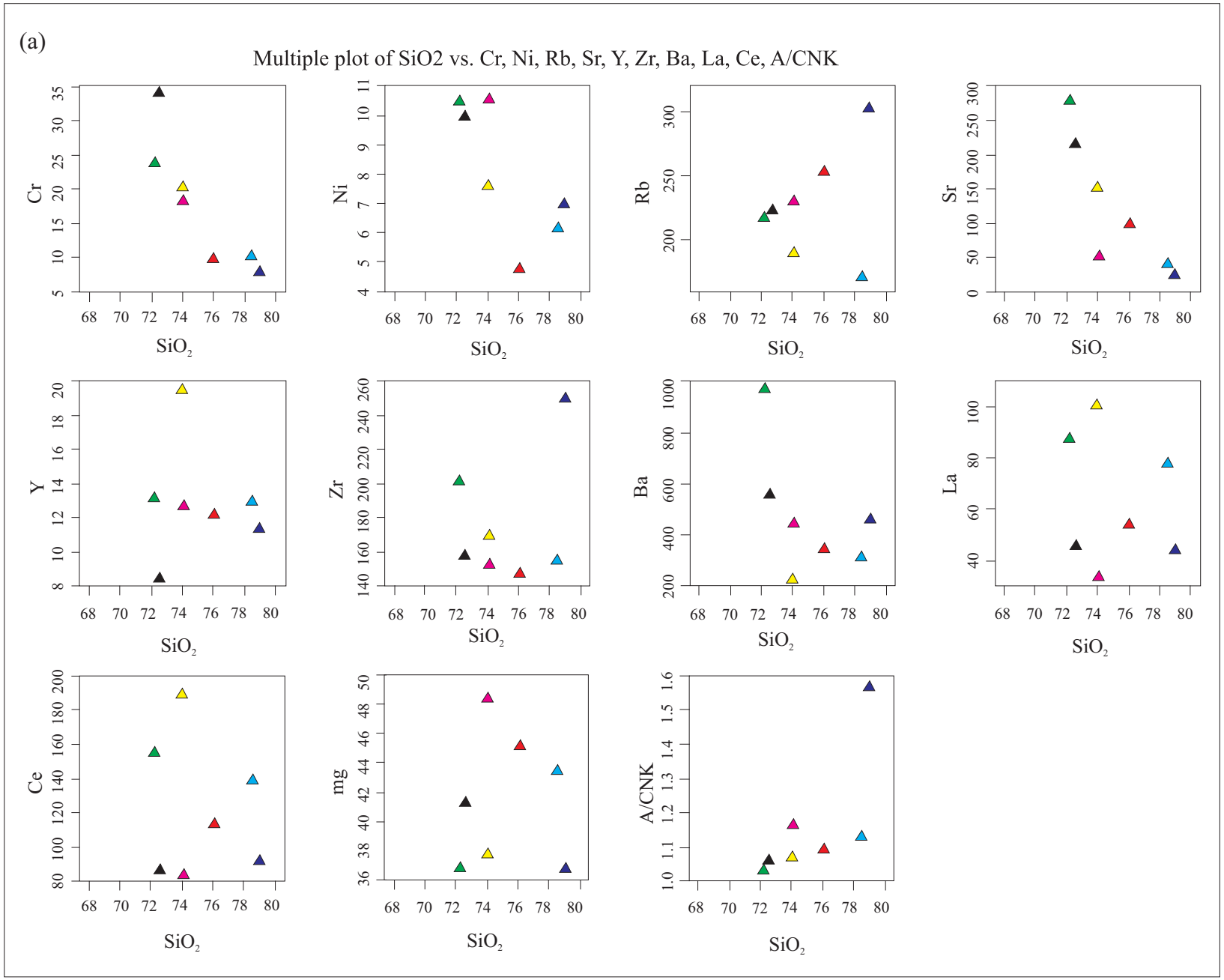

Figure. 5.4: (a) Trace element Vs SiO_2 plot shows the variation trend of the samples.

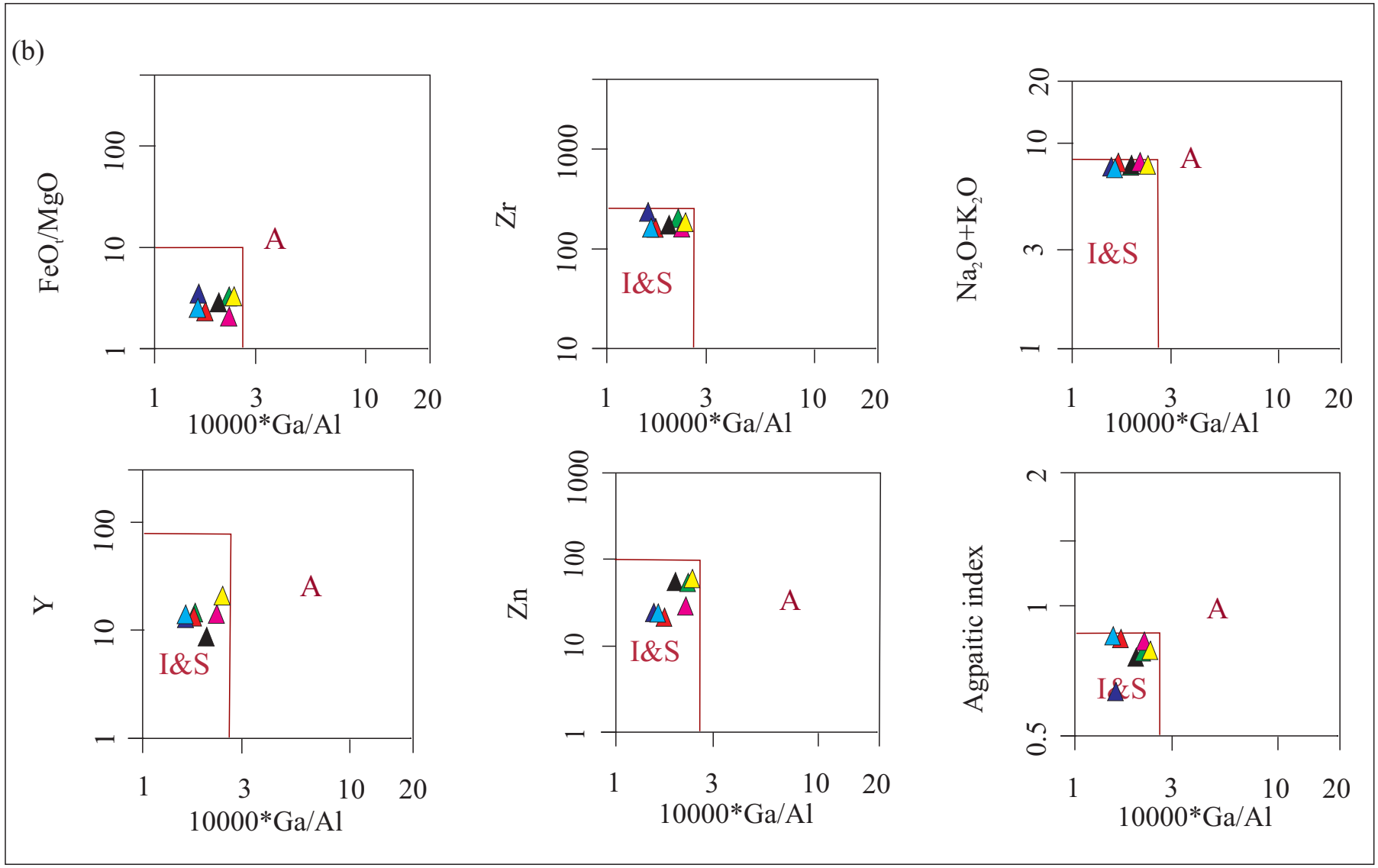

Figure. 5.4: (b) Multiple plots involving trace elements and REE of the samples: Zr vs. Ga/Al, FeOt vs. Ga/Al, Y vs. Ga/Al, Zn vs. Ga/Al, and K2O/MgO vs. Ga/Al (Whalen, 1987).

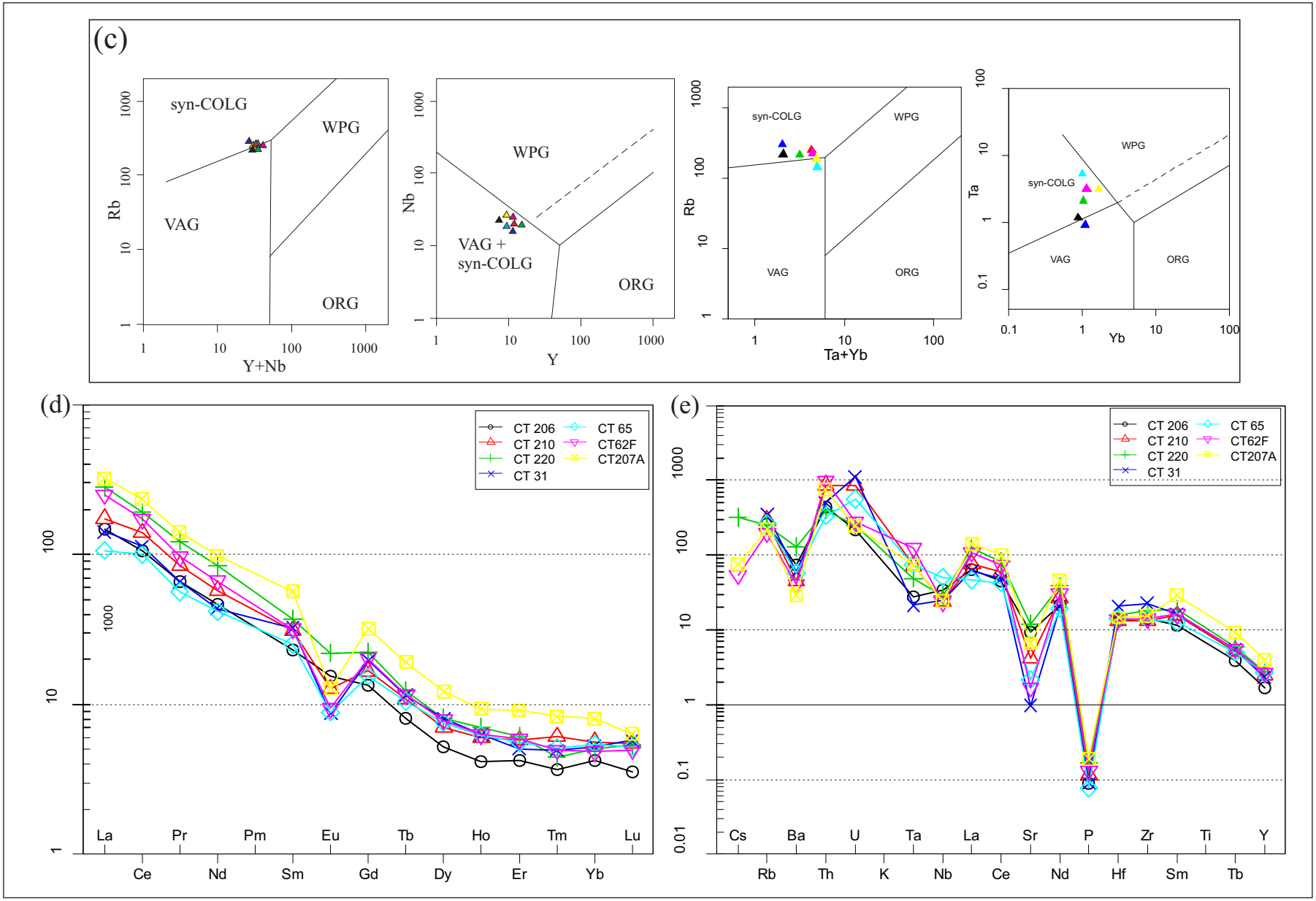

Figure 5.4. (c) Tectonic discrimination plot of Rb vs. (Y+Nb), Nb vs. Y, Rb vs. (Ta+Yb), Ta vs. Yb (Pearce et al., 1984).(d) Chondrite-normalized REE plots (Boynton, 1984) of the samples. (e) Primordial mantle-normalized REE plots (Taylor and McLennan, 1995) of the same samples.

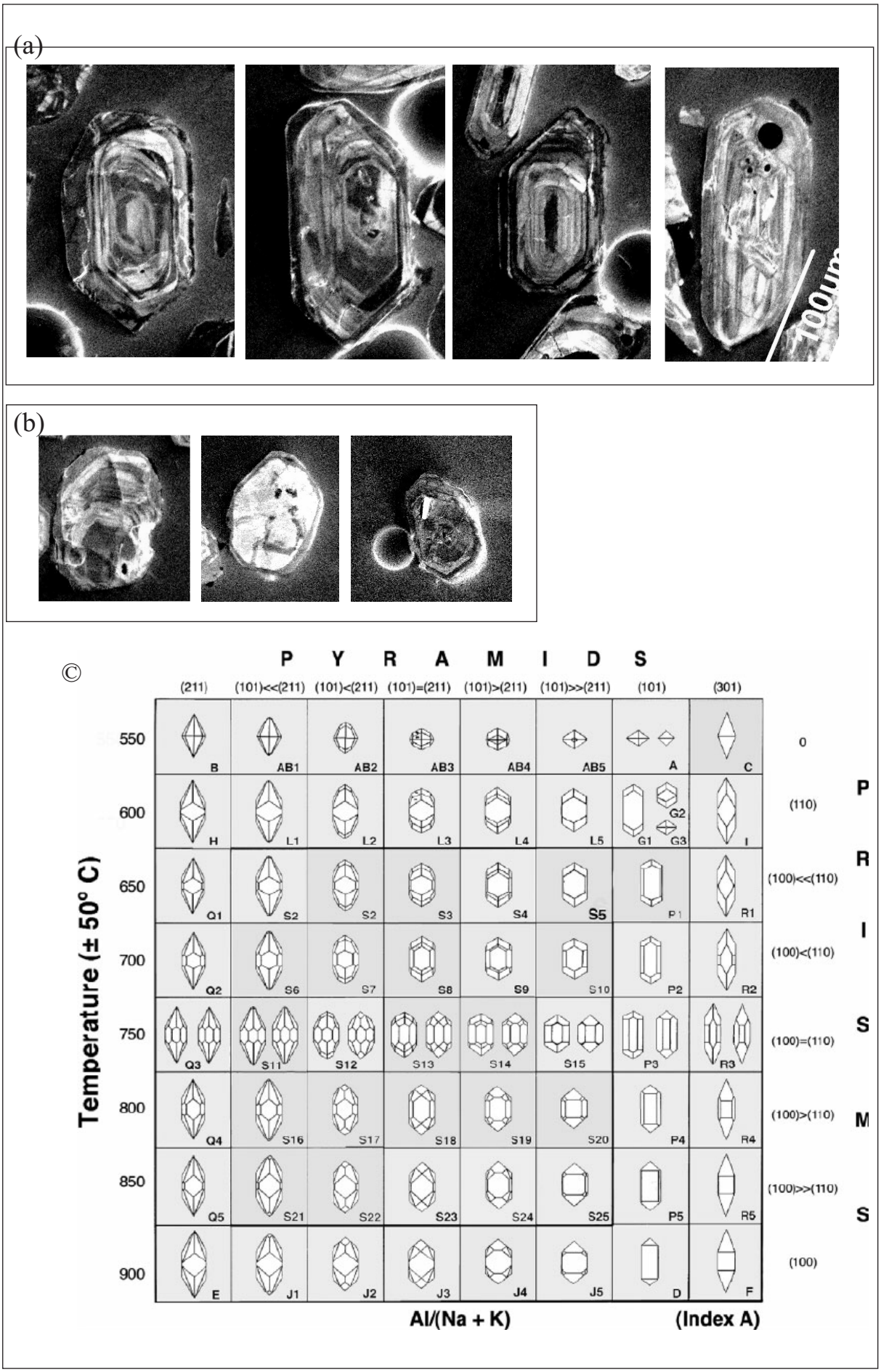

Figure 5.5. (a) Represents the type 1 zircon (b) represents the type 2 zircon (c) zircon typological classification diagram after Pupin, 1980.

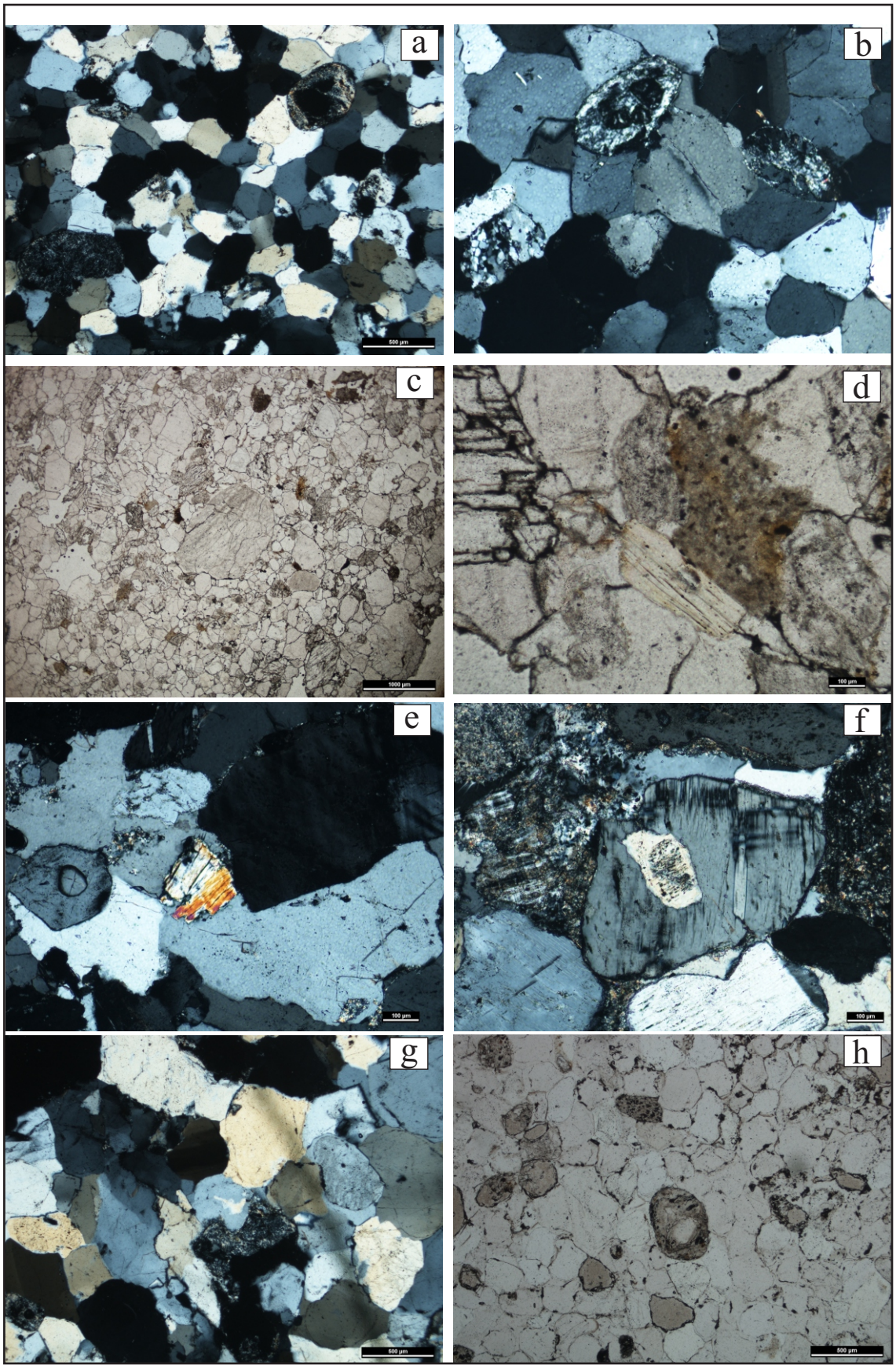

Figure 5.6. (a) Point contact presents within quartz and feldspar. (b) Quartz grains are commonly subangular to subrounded in shape. (c),(d)Intergranular fractures present within quartz, (e) Quartz grains contain inclusions of tourmaline, (f) Inclusion of quartz presents within feldspar and quartz, (g) Corroded margin presents, (h) Plagioclase feldspars are altered and illitised.

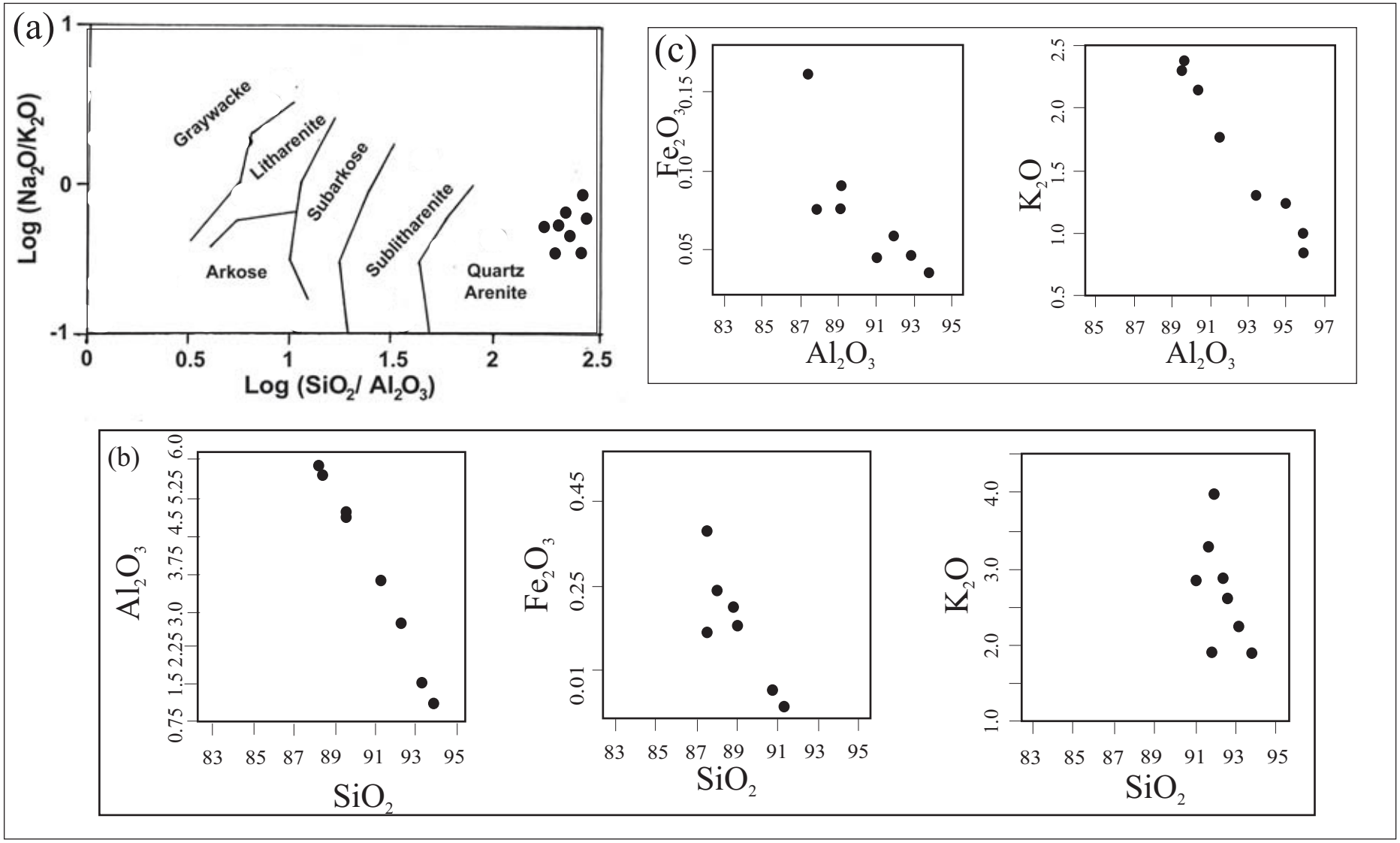

Figure. 5.7: (a) Log Na2O/K2O vs Log SiO2/Al2O3 shows all the samples plotted in quartz arenite field, (b) (c) Binary variation diagram against SiO2 and Al2O3 shows the -ve linear trend.

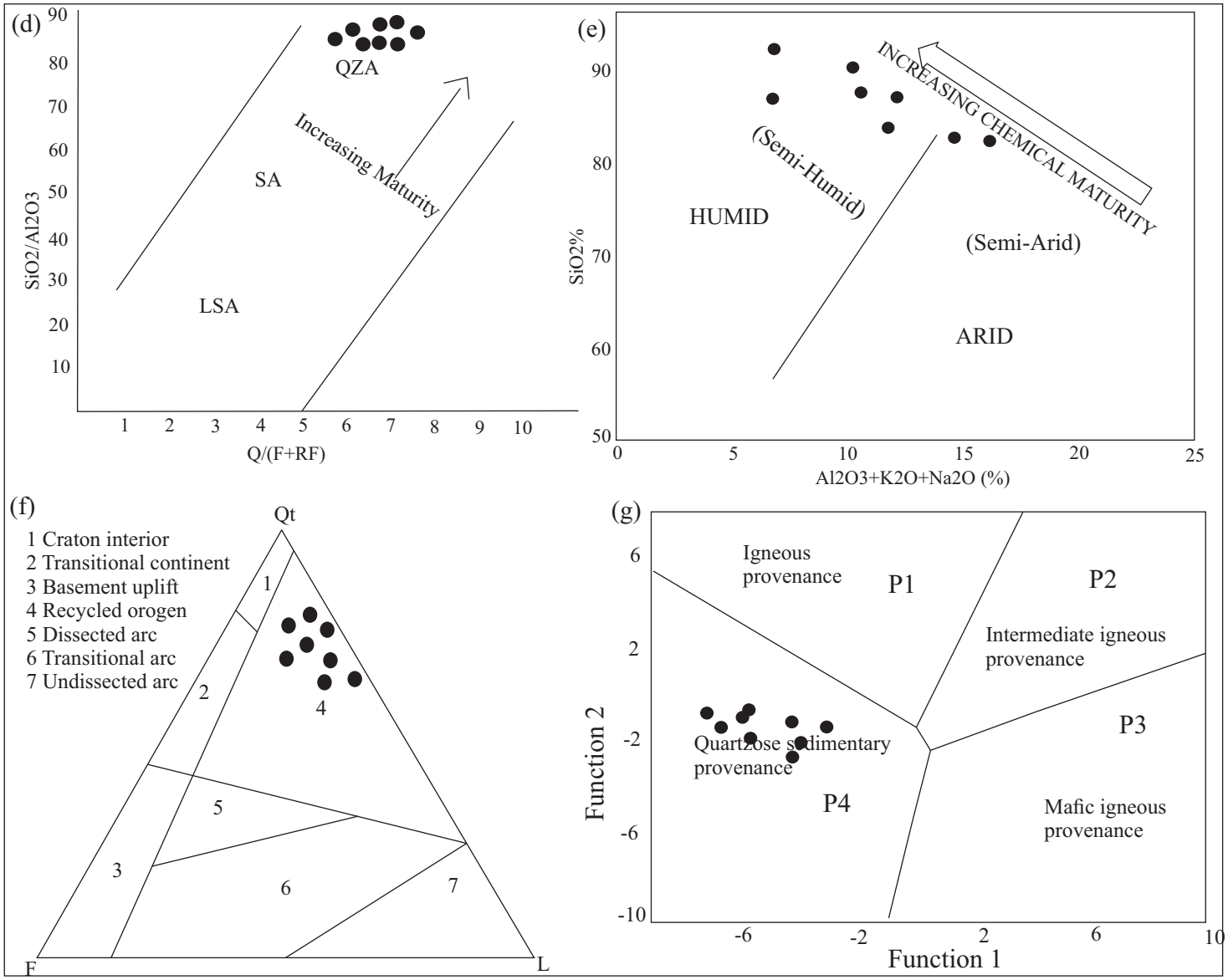

Figure. 5.7: (d) SiO2/Al2O3 Vs Q/(F+RF) after Pettijohn,1975 shows the maturity of sandstone, (e) Chemical maturity of sandstones and their palaeoenvironment of deposition based on SiO2 wt.% versus (Al2O3 + K2O + Na2O) wt.% bivariate diagram (after Suttner and Dutta, 1986). (f) Qt – F – L tectonic setting discrimination diagram (after Dickinson et al., 1983). Qt = Total quartz, F = Feldspar, L = Lithic fragments including polycrystalline quartz. (g) Provenance discrimination diagram for sandstones (after Roser and Korsch, 1988). Discriminant Function 1 = (-1.773×TiO2%) + (0.607×Al2O3%) + (0.76×Fe2O3T%) + (-1.5×MgO%) + (0.616×CaO%) + (0.509×Na2O%) + (-1.22×K2O%) + (-9.09). Discriminant Function 2 = (0.445×TiO2%) + (0.07×Al2O3%) + (0.25×Fe2O3T%) + (-1.142×MgO%) + (0.432×Na2O%) + (1.426×K2O%) + (-6.861).

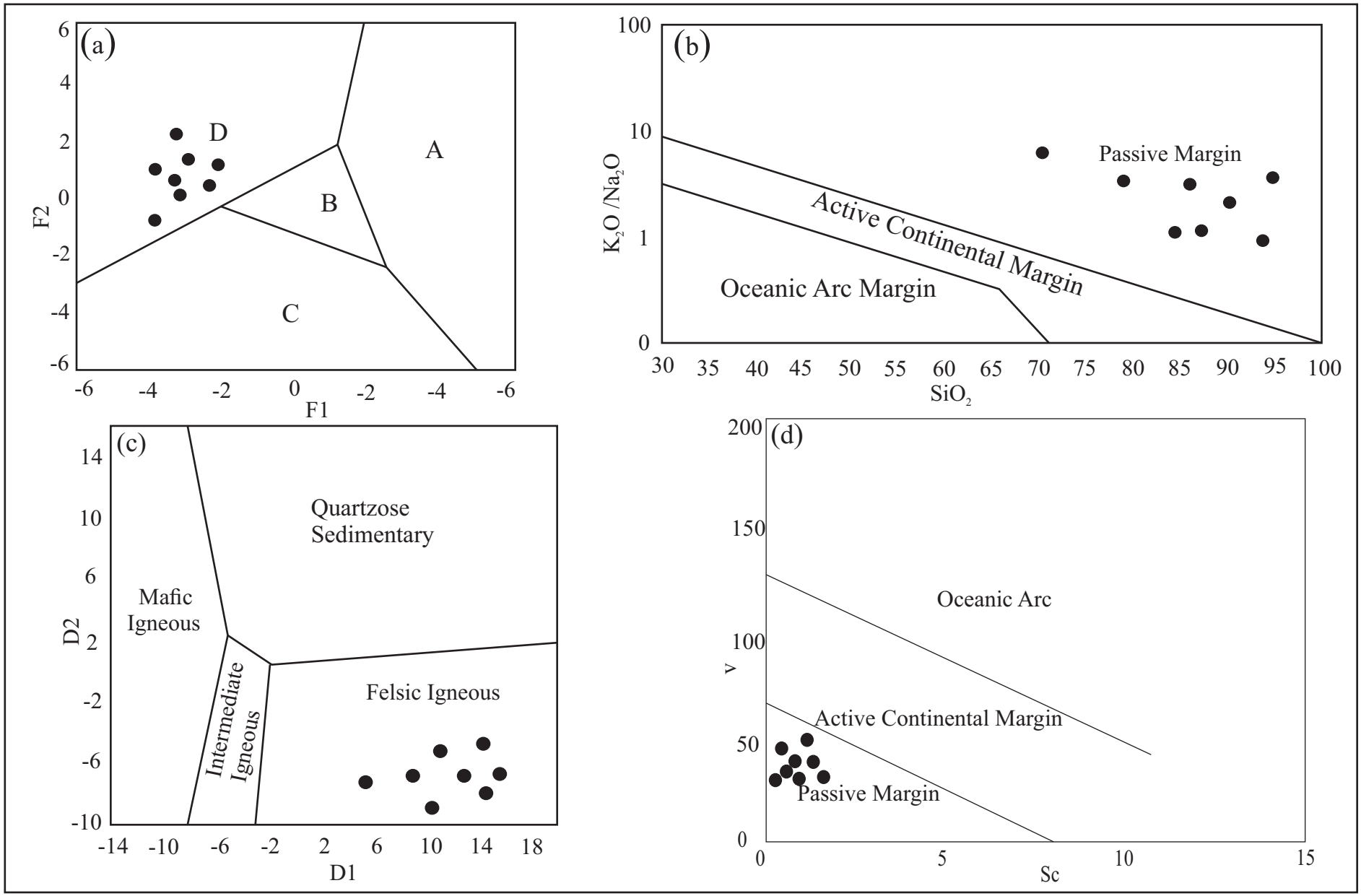

Figure. 5.8: (a) F1 - F2 classification diagram after Bhatia, 1983 where A-Oceanic Island Arc, B-Continental Island Arc, C-Active Continental Margin, D-Passive Margin. (b) K2O / Na2O vs. SiO2 provenance classification diagram after Roser and Korsch, 1986 shows the samples are the plotted within passive margin field. (c) Discriminant function diagram using major elements after Roser and Korsch, 1988. (d) Sc-V diagram shows that all the samples derived from passive margin setting (Bhatia and Crook,1986)

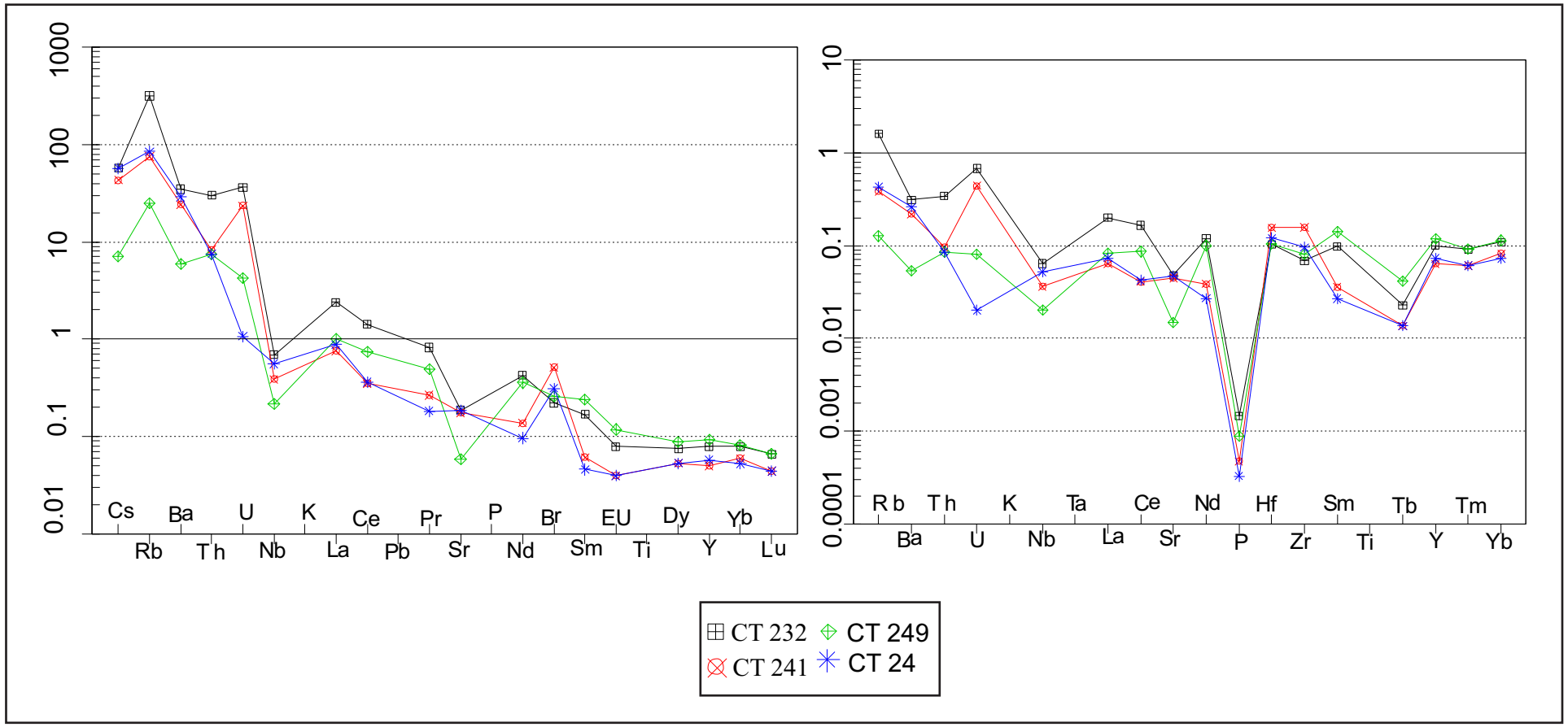

Figure.5.8: (e) Chondrite normalized plot after Sun and Mc.Dnough, 1989. (f) Upper Continental crust plot after Taylor and Mc. Lennan, 1995.

Table 5.1. A summary of location, Rock types, GPS co-ordinates,and Petrography of the studied samples.

Sample	Rock type	Lattitude	Longitude	Fabric Presents
CT4	Monzogranite	16.4963	79.0529	Pink Massive granite
CT8	Monzogranite	16.5646	78.9979	Mylonite
CT19	Monzogranite	16.5267	79.0212	Pink Massive granite
CT31	Granite	16.4737	79.0031	Grey highly fractured Massive granite
CT33	Monzogranite	16.5225	78.9217	Grey Massive granite
CT62	Monzogranite	16.5525	79.0020	Grey Massive granite
CT65	Monzogranite	16.5488	79.0045	Grey Massive granite
CT74	Monzogranite	16.5388	79.0359	Grey Massive granite
CT77	Monzogranite	16.5290	79.0222	Grey highly fractured Massive granite
CT81	Monzogranite	16.5807	79.0083	Mylonite
CT204	Monzogranite	16.5136	79.0635	Grey Massive granite
CT205	Monzogranite	16.5144	79.0800	Pink Massive granite
CT206	Monzogranite	16.5984	79.0036	Granite gneiss
CT207	Monzogranite	16.5265	79.0209	Foliated granite
CT210	Monzogranite	16.4074	79.0515	Pink Massive granite
CT211	Monzogranite	16.5299	78.9262	Porphyritic granite
CT213	Monzogranite	16.5731	78.9734	Grey Massive granite
CT217	Monzogranite	16.4812	79.0791	Foliated granite
CT219	Monzogranite	16.5429	79.0515	Grey Massive granite
CT220	Monzogranite	16.5613	79.0890	Porphyritic granite
CT227	Monzogranite	16.4658	79.0901	Pink Porphyritic Massive granite
CT229	Monzogranite	16.6467	79.2043	Grey Massive granite
CT230	Monzogranite	16.6141	79.0381	Grey Massive granite
CT230A	Monzogranite	16.6141	79.0381	Pink Massive granite
CT234	Monzogranite	16.6180	78.9678	Grey Massive granite
CT234A	Monzogranite	16.6180	78.9678	Pink Massive granite
CT237A	Monzogranite	16.5401	78.9156	Pink Massive granite
CT 1	Sandstone	16.6231	79.1561	Quartz arenite
CT23	Sandstone	16.5360	79.0261	Quartz arenite
CT24	Sandstone	16.5144	79.0302	Quartz arenite
CT209	Sandstone	16.5054	79.0439	Quartz arenite
CT214	Sandstone	16.5980	78.9841	Quartz arenite
CT232	Sandstone	16.5681	78.9836	Quartz arenite
CT241	Sandstone	78.9156	78.9725	Quartz arenite
CT249	Sandstone	16.6019	79.3044	Quartz arenite

Table 5.2. Calculated modal composition (CIPW-NORMs) of the studied granitoid samples.

Sample	Q	C	Or	Ab	An	Hy	Il	Hm	Ru	Ap	Total
CT4	38.024	2.679	22.811	28.178	3.097	1.544	0.064	1.91	0.166	0.118	98.592
CT8	40.545	4.308	24.112	23.608	0.208	2.89	0.043	1.85	0.248	0.284	98.095
CT19	32.854	1.913	25.294	31.731	4.353	1.071	0.064	1.7	0.166	0.095	99.241
CT31	49.684	4.899	43.2	1.269	0.251	0.623	0	0.86	0.22	0.071	101.041
CT33	32.901	3.726	26.771	29.024	0.866	2.865	0.043	2.41	0.218	0.189	99.013
CT62	43.099	1.369	28.934	22.754	0.424	1.4	0.028	1.453	0.165	0.116	99.742
CT65	31.963	2.12	33.207	27.306	0.969	2.399	0.046	2.039	0.209	0.183	98.441
CT74	31.124	1.161	25.057	31.731	5.35	1.893	1.107	2.09	0.244	0.237	98.995
CT77	39.967	1.641	34.808	15.908	2.648	1.221	0.021	1.25	0.099	0.047	97.61
CT81	34.245	0.035	29.726	30.716	1.702	0.772	0.021	1.17	0.115	0.426	98.928
CT204	33.136	1.218	25.294	31.478	4.091	2.167	0.086	2.23	0.215	0.189	100.104
CT205	36.601	0	31.44	24.708	3.14	1.373	0.043	1.78	0.215	0.118	99.472
CT206	29.875	0.998	26.109	30.708	7.479	2.396	0.07	2.72	0.277	0.175	100.807
CT207	33.388	1.136	24.685	30.572	5.759	1.881	0.107	2.463	0.236	0.211	100.438
CT210	36.304	1.163	30.943	25.664	2.736	1.512	0.047	1.464	0.171	0.104	100.108
CT211	36.691	2.244	23.698	29.278	2.93	1.619	0.043	1.89	0.188	0.071	98.651
CT213	32.882	0	29.608	32.239	1.434	0.394	0.064	1.13	0.212	0.284	98.255
CT217	33.775	0.567	25.471	29.785	5.313	1.769	0.086	2.32	0.185	0.142	99.413
CT219	34.218	0	29.312	30.885	0.318	1.217	0.043	1.72	0.215	0.237	98.164
CT220	28.935	0.818	30.494	28.516	6.446	1.968	0.086	2.68	0.325	0.379	100.648
CT227	37.104	2.528	30.258	26.316	1.373	1.096	0.021	0.65	0.059	0.024	99.429
CT229	33.262	1.359	31.262	30.039	0.532	1.071	0.043	1.51	0.128	0.095	99.301
CT230	34.398	1.151	33.153	28.601	0.154	1.943	0.021	1.56	0.199	0.142	101.322
CT230A	32.811	0.566	36.581	22.762	0.459	3.612	0.043	3.34	0.488	0.355	101.017
CT234	31.417	0.896	29.608	34.016	0.485	1.644	0.021	0.84	0.119	0.166	99.213
CT234A	33.591	0.527	36.936	23.016	0.145	2.043	0.064	3.41	0.316	0.379	100.428
CT237A	32.561	0.249	38.472	22.677	0.26	2.591	0.043	3.46	0.398	0.355	101.067

Table 5.3. Major element compositions of studied granitoid samples.

Sample	SiO_2	TiO_2	Al_2O_3	Fe_2O_3	MnO	MgO	CaO	Na_2O	K_2O	P_2O_5	LOI	Total
CT4	74.42	0.2	13.47	1.91	0.03	0.62	0.69	3.33	3.86	0.05	1.6	100.18
CT8	74.2	0.27	13.39	1.85	0.02	1.16	0.2	2.79	4.08	0.12	2.6	100.68
CT19	73.56	0.2	14.31	1.7	0.03	0.43	0.93	3.75	4.28	0.04	1.5	100.73
CT20	76.01	0.23	11.55	1.48	0.03	0.82	0.61	2.88	5.51	0.06	0.58	99.76
CT31	78.97	0.22	13.15	0.86	0.00	0.25	0.09	0.15	7.31	0.03	0.67	101.70
CT33	72.27	0.24	14.59	2.41	0.02	1.15	0.28	3.43	4.53	0.08	1.6	100.6
CT62	78.50	0.18	11.25	1.45	0.01	0.56	0.15	2.69	4.90	0.05	0.58	100.32
CT65	74.10	0.23	13.87	2.04	0.02	0.96	0.30	3.23	5.62	0.08	0.27	100.71
CT74	72.6	0.3	13.88	2.09	0.05	0.76	1.21	3.75	4.24	0.1	1.6	100.73
CT77	75.31	0.11	12.08	1.25	0.01	0.49	0.56	1.88	5.89	0.02	1.20	98.80
CT81	75.81	0.14	12.04	1.17	0.01	0.31	0.59	3.63	5.03	0.18	1.4	100.31
CT204	74.21	0.26	13.47	2.23	0.04	0.87	0.93	3.72	4.28	0.08	1.09	101.18
CT205	76.31	0.11	11.42	1.78	0.02	0.71	0.82	2.92	5.32	0.05	0.20	99.66
CT206	72.56	0.31	14.48	2.72	0.03	0.96	1.61	3.63	4.42	0.07	0.23	101.02
CT207	74.00	0.29	13.71	2.46	0.05	0.76	1.28	3.61	4.18	0.09	0.96	101.39
CT210	76.07	0.20	12.82	1.46	0.02	0.61	0.61	3.03	5.24	0.04	0.17	100.27
CT211	74.39	0.21	13.35	1.89	0.02	0.65	0.63	3.46	4.01	0.03	1.52	100.16
CT213	75.22	0.12	11.96	1.13	0.03	0.29	0.55	3.81	5.01	0.12	1.1	99.34
CT217	74.09	0.23	12.97	2.32	0.04	0.71	1.15	3.52	4.31	0.06	0.36	99.76
CT219	75.3	0.11	11.49	1.72	0.02	0.22	0.58	3.65	4.96	0.1	0.98	99.13
CT220	72.24	0.37	14.31	2.68	0.04	0.79	1.51	3.37	5.16	0.16	0.20	100.82
CT227	76.03	0.07	13.69	0.65	0.01	0.44	0.29	3.11	5.12	0.01	1.2	100.62
CT229	75.02	0.15	13.12	1.51	0.02	0.43	0.16	3.55	5.29	0.04	1.6	100.89
CT230	76.75	0.21	12.84	1.56	0.01	0.78	0.11	3.38	5.61	0.06	0.95	102.26
CT230A	74.5	0.51	11.86	3.34	0.02	1.45	0.29	2.69	6.19	0.15	2.3	103.3
CT234	75.16	0.13	13.11	0.84	0.01	0.66	0.19	4.02	5.01	0.07	1.1	100.3
CT234A	74.61	0.35	11.82	3.41	0.03	0.82	0.24	2.72	6.25	0.16	1.8	102.21
CT237A	74.72	0.42	11.8	3.46	0.02	1.04	0.25	2.68	6.51	0.15	1.9	102.95

Table 5.4. Trace element and REE compositions of studied granitoid samples.

Sample	CT31	CT62	CT65	CT206	CT207	CT210	CT220
Sc	3.54	1.77	5.52	3.28	6.83	3.86	4.5
V	14.48	9.29	23.9	34.1	21.45	10.56	32.64
Cr	7.87	10.03	18.13	34.62	20.14	9.57	23.65
Co	134.71	200.21	124.13	60.98	126.52	129.88	87.85
Ni	6.97	6.12	10.51	9.87	7.57	4.72	10.46
Cu	11.63	8.32	10.08	8.49	7.15	8.26	17.24
Zn	22.01	20.67	26.23	48.76	53.15	20.1	46.38
Ga	11.01	9.51	16.06	15.25	17.18	11.34	16.88
Rb	301.57	169.54	228.74	221.17	188.88	251.93	215.17
Sr	22.17	38.90	49.86	214.42	151.06	97.03	276.64
Y	11.28	12.90	12.66	8.19	19.46	12.16	13.12
Zr	249.13	154.50	152.03	156.89	168.34	146.46	201.37
Nb	15.22	14.61	31.47	21.44	14.94	14.96	17.66
Cs	bdl	1.02	bdl	0	1.42	0	6.07
Ba	457.18	308.57	439.31	552.3	222.83	340.63	974.99
La	43.80	77.37	33.02	45.48	100.28	53.83	87.11
Ce	91.58	138.99	80.86	85.70	188.32	112.93	154.60
Nd	26.11	39.80	24.92	27.74	59.21	34.49	50.28
Yb	1.10	1.01	1.13	0.89	1.68	1.17	1.04
Hf	7.18	4.81	4.95	4.70	5.15	4.61	5.44
Pb	75.48	38.88	50.48	47.32	47.98	47.48	54.94
Th	48.47	94.31	32.32	42.83	71.49	83.21	38.53
U	30.2	7.57	15.17	5.93	6.60	23.43	6.73
Ta	0.92	5.29	3.20	1.17	3.16	3.11	2.10
Pr	8.01	11.75	6.86	8.04	17.13	10.34	14.89
Sm	6.30	6.21	4.91	4.48	11.05	6.09	7.22
Tb	0.55	0.55	0.50	0.38	0.91	0.52	0.59
Mo	0.32	0.47	bdl	bdl	1.29	12.31	0.92
Eu	0.64	0.69	0.65	1.14	0.94	0.93	1.62
Gd	5.10	5.24	4.02	3.48	8.29	4.33	5.78
Dy	2.59	2.53	2.43	1.67	3.93	2.28	2.61
Ho	0.45	0.45	0.45	0.30	0.67	0.43	0.50
Er	1.06	1.23	1.18	0.89	1.92	1.21	1.28
Tm	0.16	0.16	0.17	0.12	0.27	0.20	0.14
Lu	0.18	0.16	0.17	0.11	0.20	0.18	0.17
Rb/Sr	13.60	4.36	4.58	1.03	2.15	2.60	0.77
La/Sm	6.95	12.46	6.73	10.15	9.08	8.84	12.07
La_N/Yb_N	26.64	51.07	19.43	34.17	39.79	30.63	55.65
Eu/Eu*	0.35	0.37	0.45	0.88	0.30	0.56	0.77
Sr/Y	1.97	3.02	3.94	26.18	7.76	7.98	21.09
ΣREE	187.62	286.14	161.27	180.41	394.81	228.92	327.84

Table 5.5. Zircon saturation thermometry of studied granitoid samples.

Sample	M	$Zr_{.obs}$	$Zr_{.sat}$	$T_{Zr.sat}$. (°C)	$Zr_{.sat}$ (Boehnke)	$T_{Zr.sat}$.(°C)(Boehnke)
CT4	1.14278	161	84	805	132.2	770.9
CT8	0.98316	190	73.3	834.5	109.8	811.3
CT19	1.26134	105	92.9	760	151.6	713.3
CT31	0.84468	249.13	65.2	871.7	93.5	862.6
CT33	1.11122	137	81.8	793.7	127.4	757.6
CT62	1.19482	154.5	87.8	798	140.4	760
CT65	1.24821	152.03	91.9	792.6	149.3	751.8
CT74	1.36302	158	101.3	787.4	170.6	742.1
CT81	1.44619	182	108.7	793.6	187.9	746.7
CT206	1.4042	156.89	104.9	783.7	179	736.5
CT207	1.35125	168.34	100.3	793.8	168.3	750
CT210	1.28609	156.89	104.9	783.7	179	736.5
CT220	1.44257	201.37	108.4	802.9	187.1	757.7
CT227	1.14182	161	88.4	798	144.6	775.1
CT229	1.27965	119	94.4	769.2	154.9	723.4

M- Melt composition

$Zr_{.obs}$ - Observed zircon content

$Zr_{.sat}$ - Zircon saturation composition

$T_{Zr.sat}$. (°C) - Zircon saturation temperature

Table 5.6: Recalculated framework of the Srisailam sandstone of Chitrial area.

Sample		CT 1	CT23	CT24	CT209	CT214	CT232	CT241	CT249
QFR	Q	85	86	88	91	90	85	87	93
	F	11	9	8	6	8	10	11	4
	R	4	5	4	3	2	5	2	3
QtFL	Qt	87	88	90	92	91	88	87	94
	F	11	9	8	6	8	10	11	4
	L	2	3	2	2	1	2	2	3
QmFLt	Qm	74	77	78	70	76	76	82	75
	F	12	10	8	7	8	12	11	4
	Lt	14	13	14	23	16	11	7	21
Qp LvLs	Qp	86	87	89	94	91	85	85	91
	Lv	0	0	0	0	0	0	0	0
	Ls	14	13	11	6	9	14	15	9
QmPK	Qm	84	85	86	91	84	85	88	88
	P	5	7	2	4	6	4	3	2
	K	11	8	12	4	10	9	8	10
Qp/(F+R)		**5.733**	**6.214**	**7.417**	**2.560**	**9.100**	**5.000**	**6.540**	**13.000**
Qt/(F+R)		**5.800**	**6.286**	**7.500**	**10.230**	**9.100**	**5.180**	**6.700**	**13.429**

Qt - Total quartz (Qm+Qp)
Qp - Polycystalline quartz (including chert fragments in case of QtFL)
Qm - Monocrysatlline quartz
F - Total feldspar (K+P)
K - K-feldspar
P - Plagioclase feldspar
R - Rock fragments including chert fragments
L - Total lithic fragment

Lv - Total volcanic fragments
Ls - Total sedimentary fragments
Lt- Lithic fragments + Polycrystalline quartz (Qp)

Table 5.7. Major element compositions of studied sandstone samples.

Sample	CT 1	CT23	CT24	CT209	CT214	CT232	CT241	CT249
SiO_2	94.02	91.02	92.5	90.89	94.02	93.77	94.07	97.08
TiO_2	0.01	0.01	0.01	0.01	0.01	0.01	0.01	0.01
Al_2O_3	4.06	5.45	5.98	5.73	3.65	5.87	3.78	1.95
Fe_2O_3	0.01	0.01	0.01	0.49	0.36	0.01	0.44	0.05
MnO	0.01	0.01	0.01	0.01	0.01	0.01	0.01	0.01
MgO	0.01	0.01	0.01	0.05	0.01	0.01	0.01	0.01
CaO	0.01	0.01	0.01	0.01	0.01	0.01	0.01	0.01
Na_2O	0.02	0.07	0.01	0.01	0.01	0.04	0.01	0.01
K_2O	2.48	2.09	1.63	2.43	1.45	2.54	1.45	0.36
P_2O_5	0.01	0.01	0.01	0.01	0.01	0.01	0.01	0.02
LOI	0.22	0.84	0.34	0.53	0.53	0.68	0.39	0.29

Table 5.8. Trace element and REE compositions of studied sandstone samples.

Sample	CT24	CT209	CT232	CT241	CT249
Ba	182	166	219	152	37
Be	<1	<1	<1	<1	<1
Co	229	182.4	182.6	194.3	209.3
Cs	0.4	0.3	0.4	0.3	<0.1
Ga	3.2	3.6	7.6	2.8	1.8
Hf	0.7	0.8	0.6	0.9	0.6
Nb	1.3	1.1	1.6	0.9	0.5
Rb	47.5	39.3	177.4	42.1	13.9
Sn	<1	<1	<1	<1	<1
Sr	16.6	17.1	16.8	15.6	5.2
Ta	3.5	0.8	0.6	0.8	0.8
Th	0.9	1.2	3.6	1	0.9
U	<0.1	1.2	1.7	1.1	0.2
V	<8	9	10	<8	<8
W	1682.9	1392.6	1297.9	1404.9	1573.5
Zr	23	28.8	16.4	37.7	19.2
Y	1.6	1.6	2.2	1.4	2.6
La	2.2	2.1	6	1.9	2.5
Ce	2.7	3.1	10.6	2.6	5.5
Pr	0.24	0.41	1.08	0.35	0.65
Nd	0.7	1.3	3.1	1	2.6
Sm	0.12	0.22	0.44	0.16	0.63
Eu	0.04	0.05	0.08	0.04	0.12
Gd	0.15	0.19	0.6	0.12	0.6
Tb	0.03	0.06	0.09	0.03	0.05
Dy	0.24	0.28	0.4	0.24	0.34
Ho	0.04	0.06	0.07	0.04	0.07
Er	0.17	0.18	0.23	0.16	0.24
Tm	0.02	0.02	0.03	0.02	0.03
Yb	0.16	0.19	0.24	0.18	0.25
Lu	0.02	0.02	0.03	0.02	0.03